UNIVERSITY OF LONDON THESIS

Degree PhD Year 2007 Name of Author STEPHEN PETER MALTON

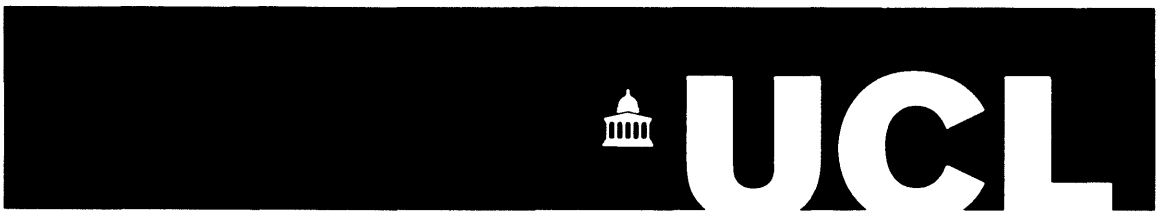

Laser Interactions with High Brightness Electron Beams

Stephen P. Malton
University College London

A thesis submitted for the degree of Doctor of Philosophy
of the University of London

Feb. 2007

ProQuest LLC
789 East Eisenhower Parkway
P.O. Box 1346
Ann Arbor, MI 48106-1346

DECLARATION

I confirm that the work presented in this Thesis is my own. Where information has been derived from other sources, I confirm that his has been indicated in the document.

Stephen Malton

Abstract

The International Linear Collider will be a high-precision machine to study the next energy frontier in particle physics. At the TeV energy scale, the ILC is expected to deliver luminosities in excess of 10^{34} $cm^{-2}s^{-1}$. In order to achieve this, beam conditions must be monitored throughout the machine. Measurment of the beam emittance is essential to ensuring that the high luminosity can be provided at the interaction point. At the design beam sizes in the ILC beam delivery system, the Laserwire provides a non-invasive real-time method of measuring the emittance by the method of inverse Compton scattering. The prototype Laserwire at the PETRA storage ring has produced consistent results with measured beam sizes of below 100 μm.

The Energy Recovery Linac Prototype (ERLP) is a technology testbed for the 4th Generation Light Source (4GLS). Inverse Compton scattering can be used in the ERLP as a proof of concept for a proposed 4GLS upgrade, and to produce soft X-rays for condensed matter experiments. The design constraints for the main running mode of the ERLP differ from those required for inverse Compton scattering. Suitable modifications to the optical lattice have been developed under the constraint that no new magnetic structures may be introduced, and the resulting photon distributions are described.

Acknowledgements

Thanks are due to many people for their help and cooperation during the course of my studies. There are far too many to name everyone individually so to those that are not listed here, I apologise and thank you.

Thanks are due to the ASTeC group at Daresbury for their technical, managerial and financial support. To Susan Smith, David Holder and Mike MacDonald especially, for taking the time out of their schedules at what has been an exceptionally busy time for them in order to answer my questions and point me in the right direction.

To the UCL HEP group, thanks for keeping me on track and sane, the ILC group for their indulgence of continual coffee breaks, and to David Miller, who has expended a great deal of effort to drive me over the final hurdles.

Finally, I would like to thank the Laser-Based Beam Diagnostics collaboration for the opportunities that have been presented to me in working with them. In particular I would like to thank Stewart Boogert for his time and effort in supervising me, and for his judicious application of both carrot and stick. This thesis could not have been written without him.

Contents

List of Figures

List of Tables

CHAPTER 1

Introduction

The International Linear Collider (ILC) will be a TeV-scale electron-positron collider. It will provide scientists with a tool to explore the fundamental nature of physics, and is intended to complement the Large Hadron Collider (LHC) in filling the gaps in and beyond the standard model of particle physics. At these high energies, the cross section of interactions generally scales as $1/(\text{energy})^2$, and so a high luminosity is required to compensate for the reduction in the number of events. The ILC is expected to deliver a luminosity of 10^{34} cm^{-2} s^{-1}. In order to achieve this, the ILC proposes colliding beams with nanometre spot sizes at the interaction point.

Such small beam spot sizes require a low transverse emittance and continuous measurement of this is necessary. This requires a number of methods. Chapter 4 decribes one of these: the Laserwire, a non-invasive beam size monitor which is currently being tested at the PETRA storage ring with a view to using such a system at the ILC. By focusing a laser beam to a small spot size and colliding this with the electron bunch, high energy photons are produced by inverse Compton scattering. The variation in signal amplitude which occurs as the laser beam is swept across the electron bunch can be

used to determine the transverse dimensions of the bunch. This requires a detailed knowledge of the properties of the laser beam at the interaction point.

The running energy of the PETRA ring means that the scattered photons are γ-rays, with an energy ranging up to 780 MeV. However, there is a desire within the light-source user community for a high brightness source of photons at a significantly lower energy than this. Using the same techniques as for the Laserwire, inverse Compton scattering on the Energy Recovery Linac Prototype (ERLP) can generate a source of photons in the soft X-ray region, up to around 30 keV. Equally importantly, by using ultra-short electron bunches and laser pulses, the scattered photon bunch can be made to have a duration of a few hundred femtoseconds. This is important for studying the behaviour of matter not just in static equilibrium, but dynamically.

The ERLP has been designed to test accelerator technologies for the 4th Generation Light Source (4GLS). In particular, it is a study of beam transport and energy recovery from an electron bunch which has been disrupted by use in a Free Electron Laser (FEL). Chapter 6 studies the modifications to the FEL-mode optics lattice that are required to make an effective inverse Compton scattering source. We examine the possible lattice configurations which will generate scattered radiation of sufficient brightness to be competitive with other available X-ray sources, and we investigate the profile of the scattered photons based on conditions in the accelerator.

CHAPTER 2

Inverse Compton Scattering

2.1 Cross-section

Compton scattering is the scattering of a photon from a free electron. We can treat the electron as being accelerated by the electric field of the photon and describe the re-radiation of photons from the electron. In the rest frame of the electron, the cross section for this interaction is described by the Klein-

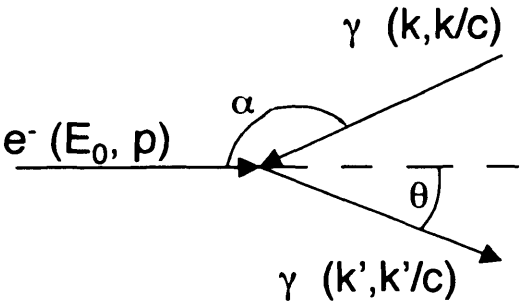

Figure 2.1: The geometry of inverse Compton scattering. A photon of energy k is incident on an electron of energy E_0 at an angle α with respect to the electron's direction of motion. After scattering, a photon of energy k' is emitted at an angle θ to the initial electron trajectory. The electron trajectory post-scattering is not shown.

Nishina formula [1]:

$$\frac{d\sigma}{d\cos\theta} = \pi r_e^2 \left(\frac{k'}{k}\right) \left[\frac{k'}{k} + \frac{k}{k'} - 1 + \cos^2\theta\right] \tag{2.1}$$

where k and k' are the energies of the incident and scattered photons respectively, and θ is the scattering angle of the photon with respect to the initial electron direction. A full derivation of this can be found in Appendix A. If the interaction is such that the recoil momentum of the electron can be disregarded, ie $k \ll m_e c^2$, then $k' \to k$, and this reduces to Thompson scattering, which gives the well-known $\cos^2\theta$ distribution of dipole radiation:

$$\frac{d\sigma}{d\cos\theta} = \pi r_e^2 \left(1 + \cos^2\theta\right) \tag{2.2}$$

which when integrated gives the Thompson cross section:

$$\sigma_{\mathrm{Th}} = \frac{8\pi}{3} r_e^2 = 0.665 \text{ barns} \tag{2.3}$$

where $r_e = 2.817939 \cdot 10^{-15}$ m is the classical electron radius.

In the case of relativistic electrons the Thompson distribution is modified by a Lorentz transformation. The approximation remains valid for interactions where the recoil momentum of the electron in its rest frame is negligible. This is true for $k \ll m_e c^2/\gamma$, and gives:

$$\frac{d\sigma}{d\cos\theta} = \pi r_e^2 \frac{1}{\gamma^2 (1 - \beta\cos\theta)^2} \left[1 + \left(\frac{\cos\theta - \beta}{1 - \beta\cos\theta}\right)^2\right] \tag{2.4}$$

where $\beta = v/c$ is the ratio of the electron velocity to the speed of light. If

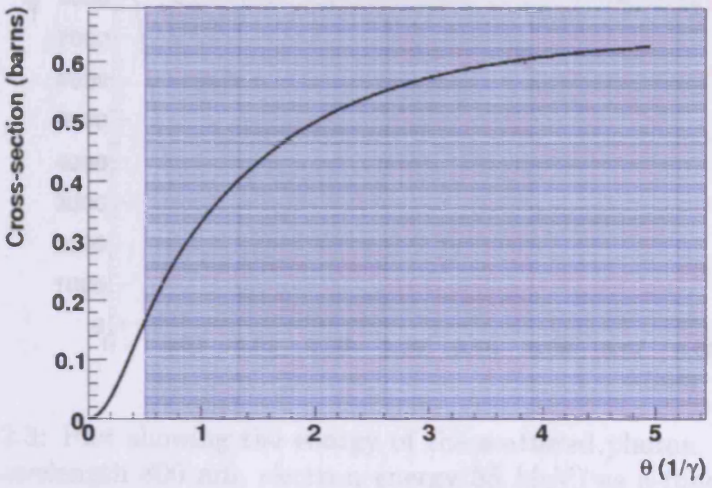

Figure 2.2: The integrated differential cross-section from Eq.2.4, as a function of half-opening angle θ (Fig. 2.1) in units of $1/\gamma$. This is the cross-section used when considering all X-rays scattered into a half-opening angle less than θ. The shaded area represents scattering into half-opening angles greater than $1/2\gamma$.

we choose to limit the integration to an opening half-angle of $1/2\gamma$, where $\gamma = E_0/m_e c^2 \gg 1$, the integral of Eq. 2.4 is numerically 0.165 barns, and is independent of the electron energy. For an electron energy of 35 MeV, the full opening angle $1/\gamma \approx 15$ mrad, which corresponds to a $\sigma_{x'}$ and $\sigma_{y'}$ of 3.5 mrad, where $\sigma_{x',y'}$ are the rms values of the $x' = \frac{dx}{ds}$ and $y' = \frac{dy}{ds}$ distributions of the particles which fall within the cone.

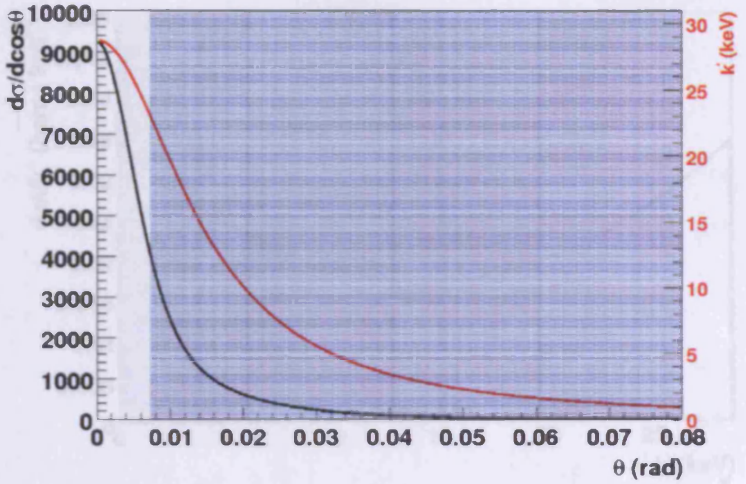

Figure 2.3: Plot showing the energy of the scattered photon, k', produced (Laser wavelength 800 nm, electron energy 35 MeV) as a function of scattering angle θ with respect to the incident electron direction (in red). Also shown is the differential cross-section $d\sigma/d\theta$ divided by $\sin\theta$ (in black). The shaded area denotes scattering angles greater than the half-opening angle $1/2\gamma$.

2.2 X-ray energy

We define the angle of incidence α and angle of emission θ of the incident and scattered photon with respect to the direction of the incoming electron, as shown in Fig. 2.1. The kinematics of the interaction can then be solved exactly to give the energy of the scattered photon [2]:

$$k' = \frac{k\left(1-\beta\cos\alpha\right)}{1-\beta\cos\theta+k\left(1+\cos\alpha\cos\theta\right)/E_0} \tag{2.5}$$

For photon energy $k \ll E_0$ where E_0 is the electron energy, this reduces to:

$$k' \simeq k\cdot\frac{1-\beta\cos\alpha}{1-\beta\cos\theta} \tag{2.6}$$

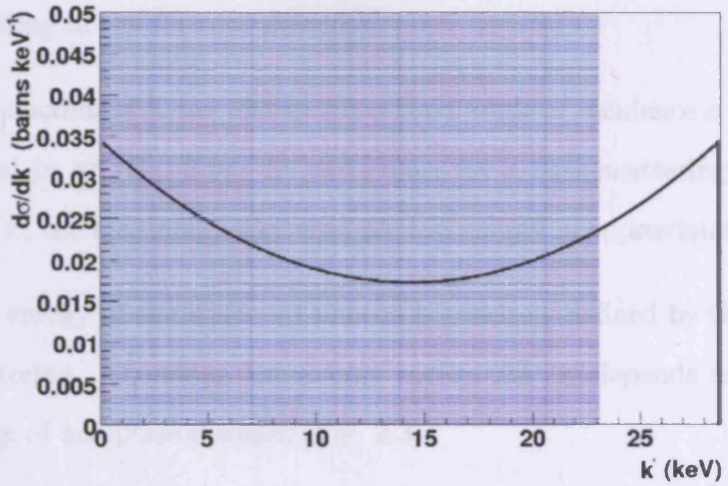

Figure 2.4: The differential cross-section from Eq. 2.7 as a function of the energy of the scattered X-ray (laser wavelength 800 nm, electron energy 35 MeV). The shaded area represents scattering into a half-angle greater than $1/2\gamma$.

The maximum energy of the scattered photon occurs for a back-scattering geometry, ie $\alpha = \pi$ and $\theta = 0$. For $E_0 \gg m_e c^2$, this gives $k'_{\max} = 4\gamma^2 k$. Taking the derivative of Eq. 2.5, we then use the chain rule to find the differential cross section with respect to the scattered photon energy (Fig. 2.4):

$$\frac{d\sigma}{dk'} = \frac{d\sigma}{d\cos\theta} \Big/ \frac{dk'}{d\cos\theta} \tag{2.7}$$

2.3 Scaling Laws

- The partial Thompson cross-section for scattering into a cone with opening half-angle of $1/2\gamma$ can be approximated as independent of γ (Fig. 2.2), *ie*, although the angle integrated over decreases for large γ, this is compensated for almost exactly by the increased Lorentz

boosting in the forward direction.

- The maximum X-ray energy for a fixed angle of incidence α is proportional to γ^2 (Eq. 2.5). In particular, for a back-scattering geometry $\alpha = \pi$, the maximum scattered photon energy is approximately $4\gamma^2 k$.

- The energy of the scattered photon is precisely defined by the angle of scattering. Therefore, the energy spread $\Delta k'/k'$ depends only on the range of acceptance angles (Fig. 2.3).

2.4 Event Rate

The number of X-rays scattered per unit time and volume is determined by the product of the electron 4-current $j_\mu(x_\nu) = ec\rho_e(x_\nu)u_\mu/\gamma$ and the photon 4-flux $\Phi_\mu(x_\nu) = c\rho_\lambda(x_\nu)k_\mu/k$ [3, 4]:

$$\frac{d^4N_\gamma(x_\nu)}{dx_\nu} = \frac{\sigma}{ec} j_\mu(x_\nu)\Phi^\mu(x_\nu) = \frac{\sigma c}{\gamma k}\rho_e(x_\nu)\rho_\gamma(x_\nu)u_\mu k^\mu \tag{2.8}$$

where $\rho(x_\nu)$ is the particle distribution function, $u_\mu = \gamma(c, \boldsymbol{u})$ is the electron 4-velocity and $k_\mu = (k, \boldsymbol{k}/c)$ is the photon 4-momentum. In Cartesian coordinates, it is possible to integrate Eq. 2.8 to explicitly calculate N_γ, the number of scattered photons per bunch crossing:

$$N_\gamma = \sigma_{\mathrm{Th}} c \left(1 - \frac{\boldsymbol{\beta}\cdot\boldsymbol{k}}{k}\right) \iiiint_{\mathcal{X}} \rho_e(x,y,z,t)\,\rho_\gamma(x,y,z,t)\,dxdydzdt \tag{2.9}$$

For a Gaussian distributed electron bunch travelling along the z-axis, we have:

$$\rho_e = \frac{N_e}{(2\pi)^{\frac{3}{2}}\sigma_x\sigma_y\sigma_z}\mathrm{Exp}\left[-\frac{(x-x_e)^2}{2\sigma_x^2}-\frac{(y-y_e)^2}{2\sigma_y^2}-\frac{(z-z_e-\beta ct)^2}{2\sigma_z^2}\right] \quad (2.10)$$

and for a flat top laser pulse with equal widths in the x and y directions travelling in the opposite direction along the z-axis:

$$\rho_\gamma = \begin{cases} \frac{P_L\lambda}{hc^2}\frac{1}{2\pi\sigma_\zeta^2}\mathrm{Exp}\left[-\frac{(x-x_\gamma)^2}{2\sigma_\zeta^2}-\frac{(y-y_\gamma)^2}{2\sigma_\zeta^2}\right] & \text{for } c(t-\Delta t) < z < c(t+\Delta t) \\ 0 & \text{for all other } z \end{cases} \quad (2.11)$$

where

$$\sigma_\gamma = \sigma_0\sqrt{1+\left[\frac{M^2\lambda(z-z_\gamma)}{4\pi\sigma_0^2}\right]^2} \quad (2.12)$$

and $(x,y,z)_{e,\gamma}$ are the positions of the electron bunch and laser pulse at time $t = 0$, $\sigma_{x,y,z}$ are the rms sizes of the electron beam, σ_0 is the waist rms of the laser spot, and $2\Delta t$ is the full duration of the laser pulse. M^2 is a numerical quality factor, where $M^2 = 1$ for a pure TEM_{00} mode laser beam, and λ is the wavelength. For $c\Delta t$ and $\sigma_z \ll z_R = \frac{4\pi\sigma_0^2}{M^2\lambda}$, we can assume $\sigma_\gamma(z) \approx \sigma_\gamma(\frac{1}{2}[z_e+z_\gamma])$ to be constant, and the integral becomes analytical. For a back-scattering geometry, *ie* $\alpha = \pi$:

$$N_\gamma = \sigma_{\mathrm{Th}}N_e\frac{P_L\lambda}{hc}\frac{\Delta t(1+\beta)}{2\pi\beta}\frac{\mathrm{Exp}\left[-\frac{(x_\gamma-x_e)^2}{2(\sigma_\zeta^2+\sigma_x^2)}-\frac{(y_\gamma-y_e)^2}{2(\sigma_\zeta^2+\sigma_y^2)}\right]}{\sqrt{(\sigma_\zeta^2+\sigma_x^2)(\sigma_\zeta^2+\sigma_y^2)}} \quad (2.13)$$

The functional form is similar for a crossing angle of $\alpha = \pi/2$, with $\sigma_x \to \sigma_z$ and $x_e \to z_e$. For $\beta \to 1$ and $\sigma_\gamma \to \sigma_{x,y}$, this becomes the standard luminosity

formula:

$$N_\gamma = \sigma_{\mathrm{Th}} \int \mathcal{L} dt = \sigma_{\mathrm{Th}} \frac{N_e N_{\mathrm{Laser}}}{4\pi\sigma_x\sigma_y} \tag{2.14}$$

Taking as an example an electron bunch containing $5 \cdot 10^8$ particles, and a laser pulse with energy 1 J at a wavelength of 1 μm, colliding with a spot size of 50 μm, we can see from Eq. 2.14 that a scattered flux of approximately $5 \cdot 10^7$ photons can be achieved.

2.5 Summary

Radiation from inverse Compton scattering has a number of defining characteristics. The peak photon energy is tunable, based on the energy of the incident electrons and the crossing angle between the electron and laser beams. The correlation between the energy of the scattered photon and its angle with respect to the initial electron energy allows selection of a desired energy bandwidth simply by restricting the angular acceptance. And the highly collimated nature of the radiation, particularly at high electron energies, generates high brightness photon beams and allows for the use of compact detectors. Each of these properties can be of use in particle accelerators. We discuss this further in the following chapters.

CHAPTER 3

ILC

The ILC is intended to operate at high luminosity in an energy range that offers an excellent opportunity of investigating new regions of physics. The technology choices for each part of the overall machine are undergoing continuous R&D to ensure that the energy and luminosity goals can be achieved under as wide a range of conditions as possible. The Global Design Effort (GDE) has produced a Basline Configuration Document (BCD) [6] which details the chosen technology for each component of the ILC, as well as the possible alternatives. As R&D continues, the recommendations in the BCD may change to take advantage of new developments.[1]

CLIC [7] is an alternative scheme for a linear collider which generates accelerating RF power from wakefield cavities sited in a conventional linac, thus avoiding the direct use of klystrons to generate high accelerating gradients. In this chapter, we limit our discussions just to the ILC; further information on CLIC can be found in [8].

[1]Feb 2007: The ILC Reference Design Report (RDR) has now been released. This thesis discusses the specifications prior to the RDR – for an up-to-date version after cost optimisation, please consult the RDR[5].

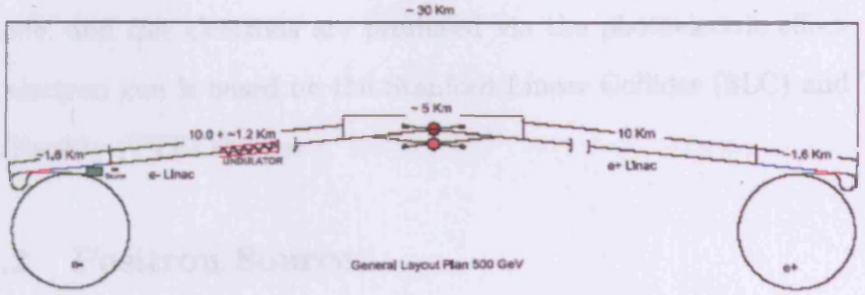

Figure 3.1: Generic design for a linear collider

3.1 Linear Collider Layout

A linear collider is composed of several sections, each with its own specific task and design requirements. Fig. 3.1 shows a generic collider layout. The beam is generated at a low energy source before being accelerated to a damping ring. This reduces the beam's initial emittance. The beam is then passed to the linear accelerator (linac) section where its energy is increased to the nominal value, before being transported through the beam delivery system (BDS) to the interaction point (IP). After the IP, the beam is guided through an extraction line to the dump. With accelerating gradients of 35 MeV/m, a 1 TeV centre of mass energy machine requires approximately 15 km of linac for each beam, making the total length of the machine, including BDS, in excess of 30 km.

3.1.1 Electron Source

The ILC specification requires that the electron source can provide better than 80 % polarisation. To acheive this, the source will be a laser-driven electron gun [9]. In this system, a laser is fired at a GaAs or Cs_2Te photo-

cathode, and free electrons are produced via the photoelectric effect. The ILC electron gun is based on the Stanford Linear Collider (SLC) and Tesla Test Facility (TTF) sources.

3.1.2 Positron Source

Positrons are generated by firing electrons or photons at a target to induce production of e^+/e^- pairs. The positrons can then be separated from the electrons in a magnetic field before being pre-accelerated and passed into a damping ring. The ILC community has chosen to use photons on the target, and these photons will be generated by passing 150 GeV electrons through a helical undulator in the main electron linac. Both permanent magnet and superconducting undulators are being considered [10].

3.1.3 Damping Rings

Damping rings are used to decrease the transverse emittance of the beams through radiation cooling. This is crucial in attaining the small spot sizes required at the IP. The emittance is reduced because the circulating electron beams emit synchrotron radiation. The overall momentum reduction that this causes can be compensated for by controlled re-acceleration. The net effect is a reduction in the transverse momentum spread. The ILC damping rings are planned to be approximately 6 km in circumference, and will receive the beam from the electron system at 5 GeV [11]. After damping, the beam will be passed into the Ring-to- Main-Linac (RTML) section, where it will undergo bunch compression and be accelerated to 13–15 GeV as required by

the pre-linac.

It has recently been decided that the electron and positron damping rings will share a common tunnel centred on the interaction region, (see Fig. 3.2).

3.1.4 Main Linac

This makes up the majority of the length of the collider. The main linac section contains accelerating structures, beam instrumentation and tune-up dumps. The ILC community has decided to use superconducting RF cavities in the main linac [12]. This will accelerate the beam from 13–15 GeV to the final collision energy. In the first instance this will be 250 GeV.

3.1.5 Beam Delivery System

The beam delivery system transports the beam from the main linac to the interaction region. It contains post-linac collimators to remove any halo of errant particles which may cause backgrounds or machine protection issues, as well as beam diagnostics and feedback systems to optimise the delivered luminosity. The current basline design is for a BDS which contains a beam switchyard [13]. This would allow the beam to be delivered to two separate interaction regions, as well as a fast-extraction line for machine protection and commisioning.

3.1.6 Interaction Region

The two beams are focused to nanometre spot sizes by the final focus quadrupoles and collide in the Interaction Region. This area is surrounded by a detector

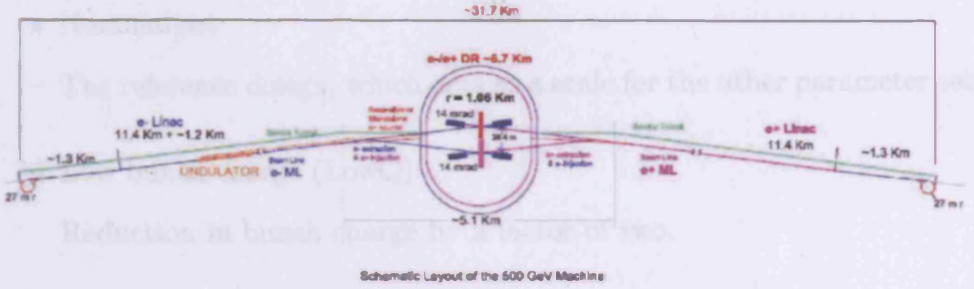

Figure 3.2: Current ILC basline design (Jan 2007) [6].

to study the collision results. The ILC currently plans to have two interaction regions in which the electron and positron paths cross at an angle of 14 mrad.

3.1.7 Extraction Line

After collision, the beams must be safely transported to dumps capable of absorbing the high power levels — up to 18 MW. In this area there are more diagnostic regions to determine the beam parameters at the IP. The crossing angle in the interaction region has a large impact on the design of the extraction line [14].

3.2 Machine Parameters

The proposed beam parameters are grouped into several sets. The idea is to have a range of available options in which the design luminosity can be achieved. This will result in a greater operational flexibilty than if the machine were designed to a single parameter set. The selected options are:

- Nominal set:

  The reference design, which acts as a scale for the other parameter sets.

- Low bunch charge (LowQ):

  Reduction in bunch charge by a factor of two.

- Large σ_y^* (Large Y):

  Increased vertical beam size due to larger emittance growth during low energy transport.

- Low power (LowP):

  Reduced number of bunches by factor of two.

- High luminosity (HighL):

  Reduced IP beam size and bunch length. This is not part of the baseline configuration.

The nominal and extreme values within these parameter sets are described in Table 3.1.

Beam and IP Parameters

		Min	Nominal	Max	
Bunch Charge	N	1	2	2	$\times 10^{10}$
Number of bunches	n_b	1330	2820	5640	
Linac bunch interval	t_{sep}	154	308	461	ns
Train repetition rate	f_{rep}	5	5	5	Hz
Bunch length	σ_z	150	300	500	μm
Horizontal emittance	$\gamma\epsilon_x$	10	10	10	mm mrad
Vertical emittance	$\gamma\epsilon_y$	0.03	0.04	0.08	mm mrad
IP beta (500 GeV)	β_x	10	21	21	mm
	β_y	0.2	0.4	0.4	mm
IP beta (1 TeV)	β_x	10	30	30	mm
	β_y	0.2	0.3	0.6	mm

Table 3.1: Parameters for the ILC design. [6]

CHAPTER 4

Laserwire

4.1 Emittance and Luminosity

The distribution of a beam of particles in transverse phase space evolves as a function of the beam's transport through the system. By defining an ellipse in x-x' space, where $x' = \frac{dx}{ds}$, such that 95% of the particles are contained, we can define a quantity, which we call the emittance ϵ, as a measure of beam quality [15]:

$$\int_{ellipse} dx\, dx' = \pi\epsilon \tag{4.1}$$

An emittance is defined in both the horizontal and vertical planes. According to the Liouville theorem, if only focussing and bending forces are applied to the beam the area of the phase space ellipse remains unchanged, and so the emittance is an invariant under these conditions. Where the particle momentum is not constant, we define the normalised emittance ϵ_n in terms of the relativistic beam parameters β and γ such that:

$$\epsilon_n = \beta\gamma\epsilon \tag{4.2}$$

The path of a particle in a beam transport system is defined by its beta function $\beta(s)$, where s is the particle's distance along the beamline. The β-function comes from solving the equations of transverse motion such that:

$$x''(s) + K(s)x(s) = 0 \tag{4.3}$$

$$x(s) = \sqrt{\epsilon}\sqrt{\beta(s)}\cos(\psi(s) - \theta) \tag{4.4}$$

$$\text{and } \frac{d\psi(s)}{ds} = \frac{1}{\beta(s)} \tag{4.5}$$

where $K(s)$ is an arbitrary function of s dependent on the particular distribution of focusing along the beamline. The phase of the oscillation at a given position s is given by $\psi(s) - \psi_0$, where ψ_0 is the initial phase and $\psi(s)$ is given by Eq. 4.5. The phase advance of a particle is then given by $\mu = \psi(s) - \psi(0)$. The beta function which then encloses those of all the particles within the phase space ellipse defining the emittance is the amplitude function, and together with the emittance this defines the beam envelope:

$$\sigma_{\text{beam}}(s) = \sqrt{\epsilon_B \cdot \beta(s)} \tag{4.6}$$

This determines the luminosity of the colliding beams at the interaction point:

$$\mathcal{L} \propto \frac{1}{4\pi\sigma_x\sigma_y} \propto \frac{1}{4\pi\sqrt{\epsilon_x^*\beta_x^*}\sqrt{\epsilon_y^*\beta_y^*}} \tag{4.7}$$

for two colliding bunches which are Gaussian in the x- and y-directions, as shown in Eq. 2.14, where the star denotes that the parameter values are at the IP.

4.2 Emittance Measurements

The emittance is a measure of both the size and divergence of the beam, and so cannot be directly measured. In clear drift space, the phase-space ellipse naturally rotates. By measuring the beam size at a number of locations, different parts of the ellipse can be measured and combined to determine the emittance (see Fig. 4.1).

In a standard wire-scanner, a series of wires is passed through the beam. This generates a profile based on either induced current in the wires from secondary emission [17], or on the flux of bremsstrahlung. In either case, the

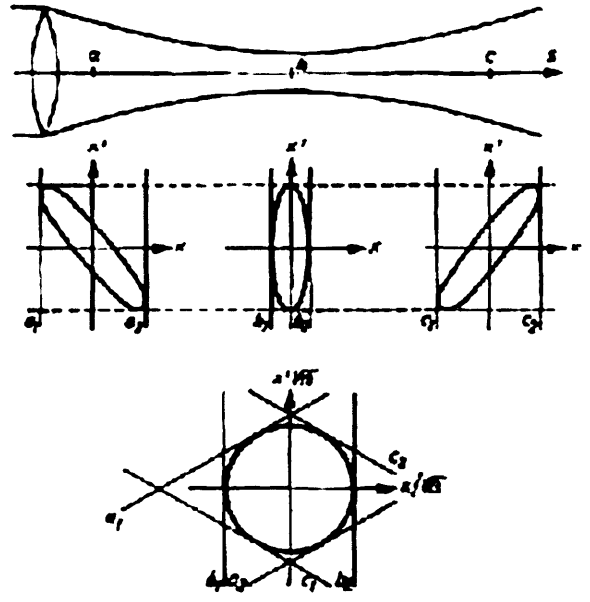

Figure 4.1: Measuring the beam transverse emittance using a series of laser-wires. Top: The beam width is measured at the waist (location b) and either side of it (locations a and c)f a waist. Bottom: As the area of the phase-space ellipse remains invariant under conservative forces, these three measurements can then be combined to determine the emittance [16].

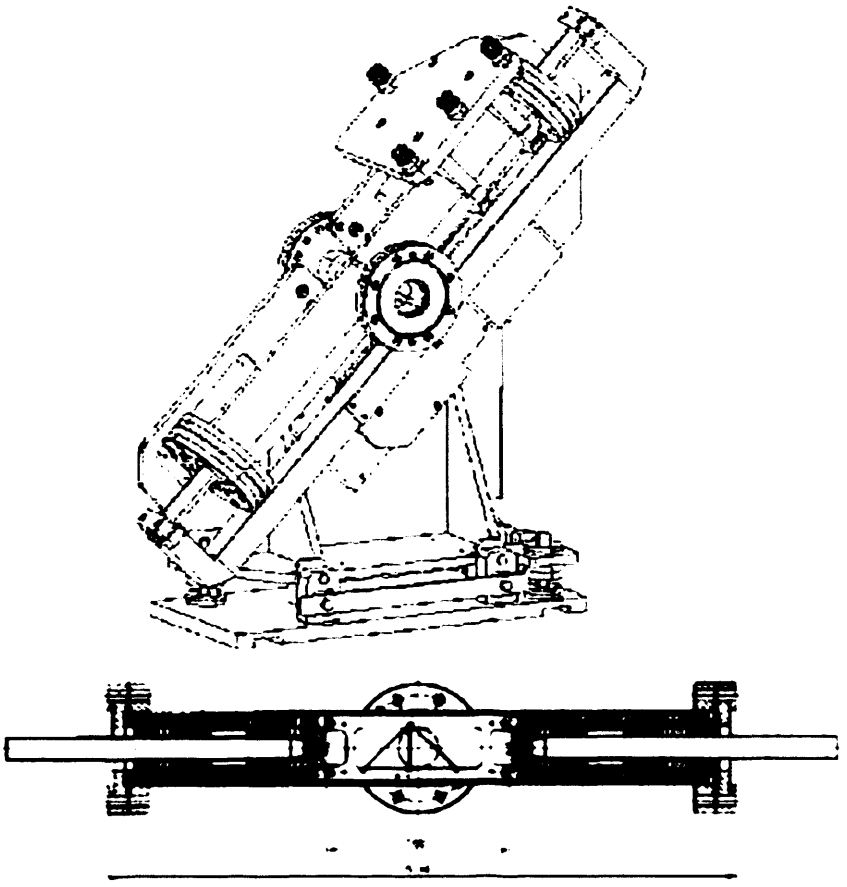

Figure 4.2: Diagram of a wirescanner beam size monitor. This scanner is installed in the TTF beamline [18].

intensity is proportional to the beam density at the wire position. By using several wires set at different angles (as in Fig. 4.2), the full profile of the beam can be measured in one location.

This approach requires that the diameter of the scanning wires be smaller than the expected beam size. Given that such wires can be manufactured down to approximately 10 μm, the use of this technique in machines where the expected beam sizes are smaller, such as the designs enumerated in Ta-

	CLIC	NLC/JLC	TESLA
BDS $\sigma_x(\mu m)$	3.4–15	7–50	20–150
$\sigma_y(\mu m)$	0.35–2.6	1–5	1–25
IP σ_x^*(nm)	196	355	535
σ_y^*(nm)	4.5	4.5	5

Table 4.1: Anticipated transverse beam sizes in the Beam Delivery System and at the Interaction Point for the CLIC [19], NLC [20] and TESLA [21] designs.

ble 4.1, is prohibited. Additionally, scanning a physical wire through the beam is immensely disruptive to the beam itself, and requires many bunches to make a measurement. Finally, at high brightness and small spot sizes as for the ILC, the wires would be destroyed.

4.3 Principles of the Laserwire

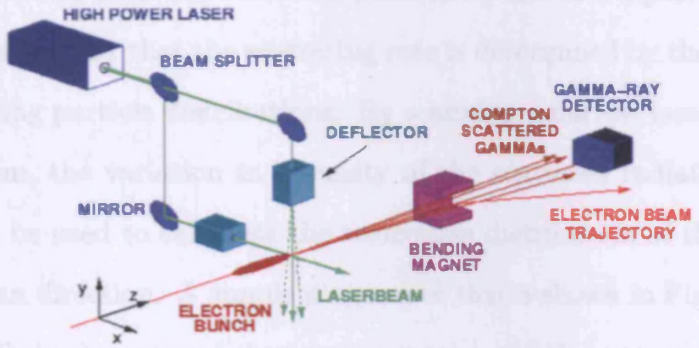

Figure 4.3: A simple schematic of the laserwire.

In a Laserwire system, the physical wire of a traditional wire scanner is replaced by an intense laser beam. As the lepton beam collides with the laser light, γ-rays are produced by inverse Compton scattering. These photons are

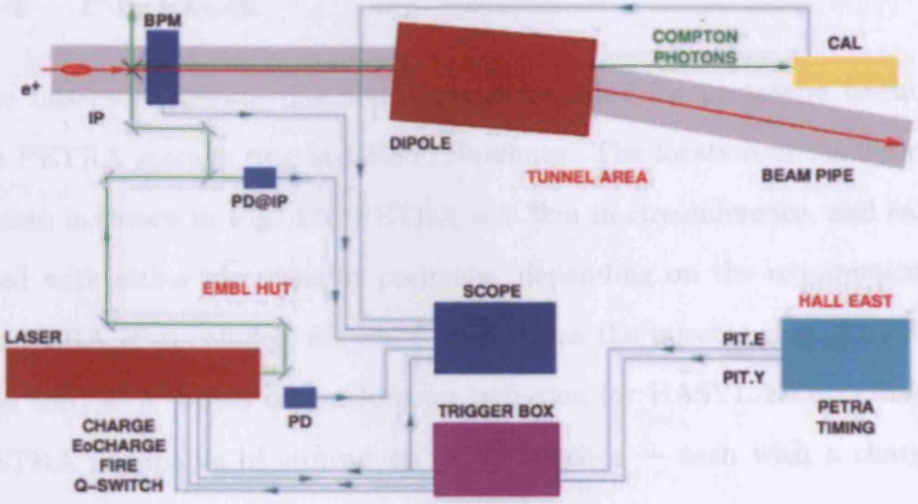

Figure 4.4: A schematic showing the connections between various sections of the laserwire system.

preferentially scattered along the axis of the lepton beam (Eq. 2.4, Fig. 2.2), which is separated from the scattered photons by use of a dipole magnet. It was shown in Sec. 2.1 that the scattering rate is determined by the integral of the overlapping particle distributions. By scanning a narrow laser across the electron beam, the variation in intensity of the scattered radiation at each position can be used to calculate the transverse distribution of the electrons along the scan direction. A simple diagram of this is shown in Fig. 4.3, while a more detailed schematic of the interconnections of the system can be seen in Fig. 4.4.

4.4 PETRA

The Laserwire system described here is installed for prototype testing in the PETRA storage ring at DESY, Hamburg. The location of the laserwire system is shown in Fig. 4.5. PETRA is 2.3km in circumference, and can be filled with either electrons or positrons, depending on the requirements of the HERA $e^{\pm}$-p collider, for which it serves as the injector ring. PETRA is also used as a source of synchrotron radiation for HASYLAB experiments. PETRA is capable of storing up to 40 bunches — each with a charge of

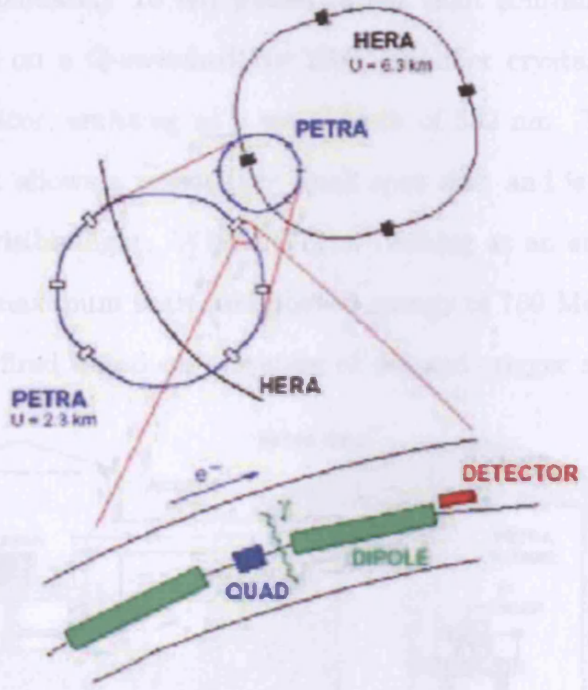

Figure 4.5: The laserwire experiment is located upstream of Halle Ost at PETRA. The interaction point occurs just before a dipole magnet. This serves to bend the electron path away from the detector, and also allows the detector to be placed outside the vacuum for ease of access.

approximately 10^{10} leptons — with a minimum bunch spacing of 96 ns. The lifetime of the bunch train is approximately 10 hours. Bunch lengths are typically 100 ps, and the bunch energy spread is approximately 0.075 % at energies of 4.5, 7 or 12 GeV.

4.5 Laser

The laser is a Quantel YG580 pulsed laser, originally used as part of the LEP polarimeter [22]. It provides high power (approximately 10 MW), short duration (approximately 10 ns) pulses rather than continuous light. The system is based on a Q-switched Nd:YAG amplifier crystal with a second harmonic generator, emitting at a wavelength of 532 nm. This wavelength was chosen as it allows a reasonably small spot size, and is simpler to deal with than non-visible light. With PETRA running at an energy of 7 GeV, Eq. 2.5 gives a maximum scattered photon energy of 780 MeV.

The laser is fired based on a system of delayed trigger signals from the

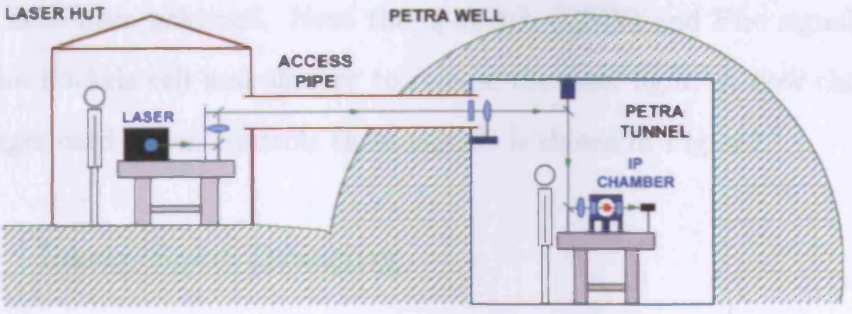

Figure 4.6: The laser is located in a hut outside the PETRA tunnel. The light is transported via a lens relay and mirror system down a 9 m long access pipe to a piezo-electric scanning mirror and focusing lens close to the interaction chamber.

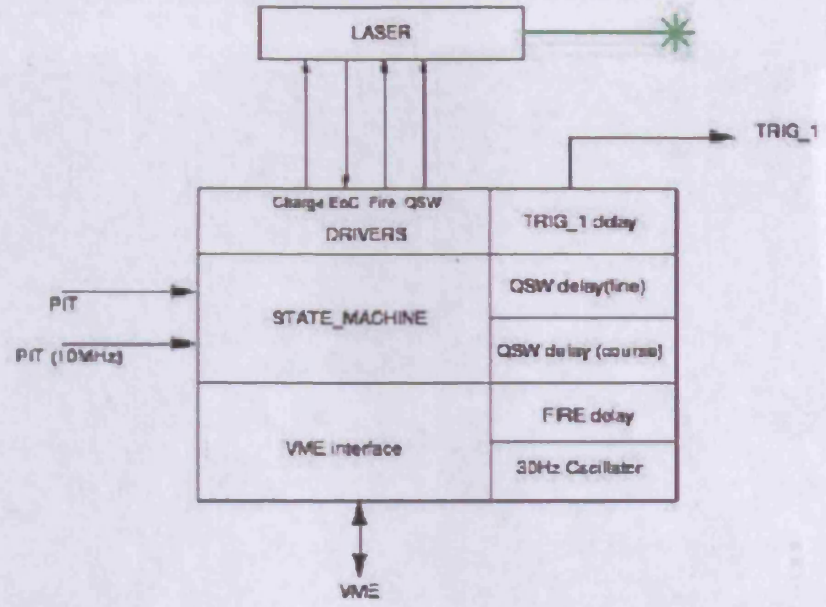

Figure 4.7: Input/output scheme for the laser trigger card.

Petra Integrated Timing (PIT) signal. First a Charge signal is sent to the laser in order to pump the gain medium using xenon flash-lamps. An End of Charge (EoC) signal is generated when a sufficient population inversion should have been achieved. Next the Q-switch (QSW) and Fire signals operate the Pockels cell and shutter to release the laser light. A flow chart of the trigger card which controls these signals is shown in Fig. 4.7.

4.5.1 Laser Spot Imaging

The laser is focused at the interaction point by a LAP125 lens. This is an air-spaced doublet lens with a back focal length of 117 mm. For diagnostic purposes, the laser light is attenuated and focused onto the chip of a Basler

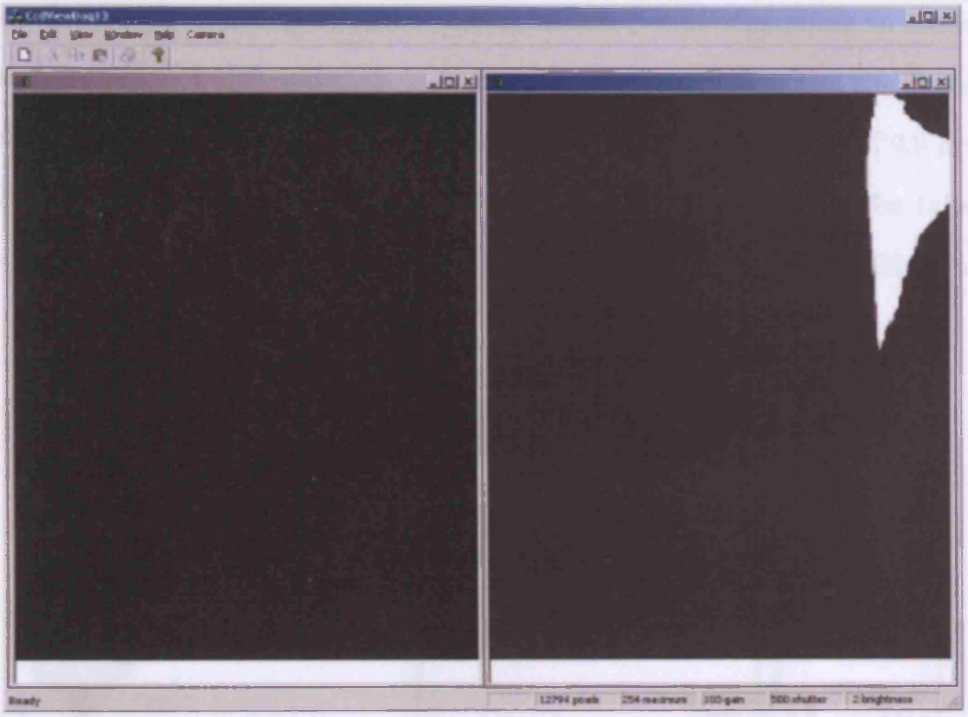

Figure 4.8: Screenshot from the CCD DAQ software. The status bar contains statistics for the camera image which has focus. The white mark on the right-hand window is laser damage to the CCD chip due to inadequate attenuation

A302f CCD camera. This has 782 × 582 pixels with a size of 8.3 × 8.3 μm each. The camera is read out over an IEEE1394 Firewire bus by a PC running Windows 2000(SP4). The imaging software shown in Fig. 4.8 is written in Visual C++. Images from multiple cameras could be captured at a rate of 25–30 frames per second, and are written to disk as bitmap files for offline analysis.

Due to the laser damage to the CCD camera (as evidenced in Fig. 4.8) and the harsh conditions in the PETRA tunnel, the CCD cameras did not have a sufficient lifespan. It was decided that a replacement system should be

installed which would be radiation-hard and less power-consuming to reduce the possibility of heat-induced damage. The camera chosen was the Basler A601f. This uses a CMOS chip with 656×491 pixels, with a pitch of 9.9 μm. All further references to "CCD", "CMOS" and "camera" should be taken to refer to the A601f. To determine how the finite pixel size would affect

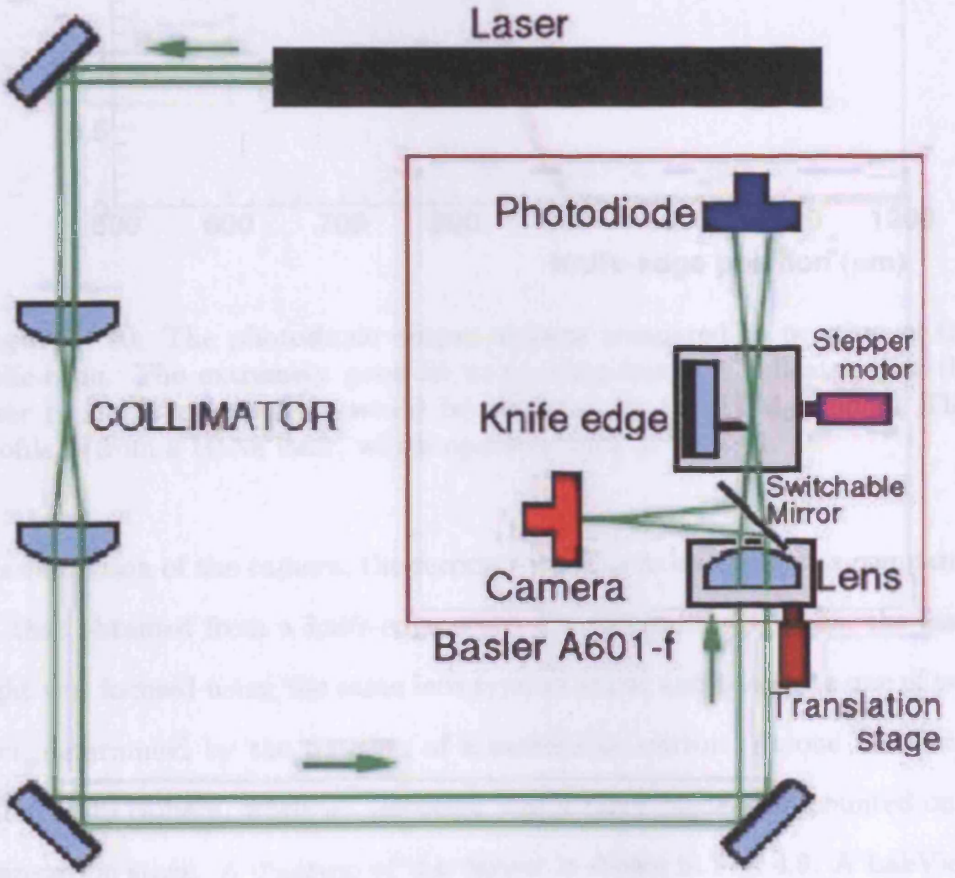

Figure 4.9: Setup of the knife scan measurements. The position of the lens controls the size of the beam seen at the two foci. A switchable mirror can be inserted or removed to determine to which focus the beam is delivered.

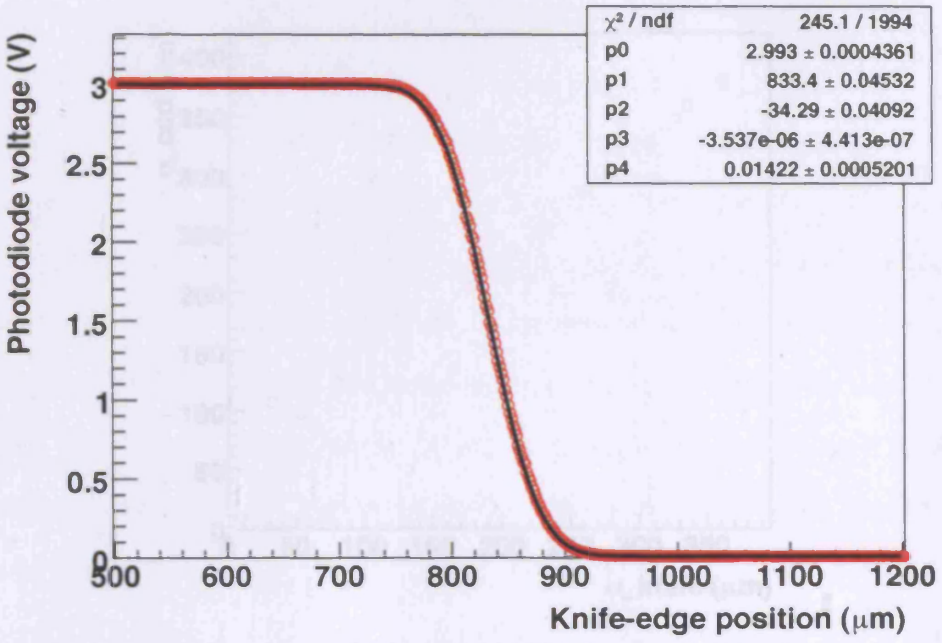

Figure 4.10: The photodiode output voltage compared to position of the knife-edge. The extremely good fit to an error-function indicates that the laser profile is gaussian, as would be expected for the TEM_{00} mode. This profile is from a HeNe laser, which operates with $M^2 < 1.01$.

the resolution of the camera, the reconstructed focus spot size was compared to that obtained from a knife-edge scan. For the knife-edge scan, the laser light was focused using the same lens type as above and passed to one of two foci, determined by the position of a switchable mirror. At one focus was the CMOS camera, while at the other was a razor blade was mounted on a translation stage. A diagram of this layout is shown in Fig. 4.9. A LabView [23] control program stepped the blade through the focus of the laser beam, and the transmitted intensity of laser light was measured using a photodiode. The measured intensity at the photodiode obeys:

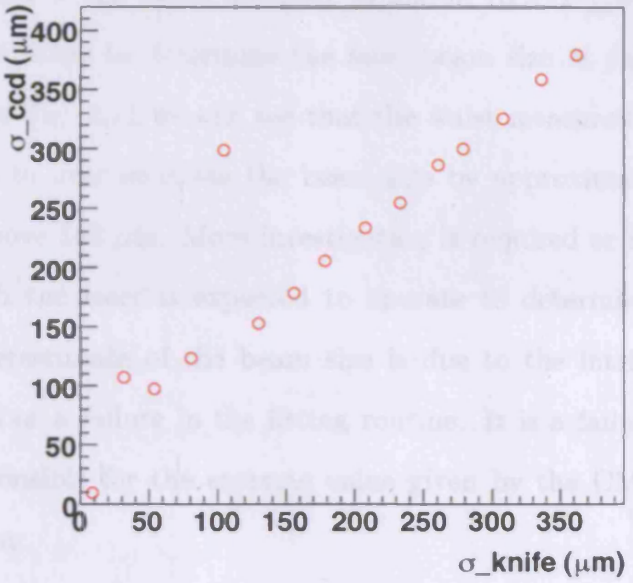

Figure 4.11: Comparison of laser beam sizes measured by knife-edge scan and CCD camera. The beam size measured by the CCD camera tends to exceed that measured by the knife-edge scan.

$$I \propto \frac{1}{2}\left[1 \pm \mathrm{Erf}\,(z)\right] \tag{4.8}$$

Fitting to this, we then obtain a value for the laser beam focus rms spot size which can be compared to the value obtained from the CMOS camera. An example fit is shown in Fig. 4.10. In this case the best fit is to a beam size of 34.29 μm. Parameters $p3$ and $p4$ are coefficients for linear and constant backgrounds respectively. The focussing lens was also mounted on a translation stage. By altering the position of the lens, the location of the focus could be moved equally at each measurement station, allowing a range of beam sizes to be be measured and compared.

The bitmap files from the camera DAQ software were used to generate

a 2D histogram of the beam intensity profile in ROOT (v4.02) [24]. This could then be fitted to determine the laser beam size as measured by the camera. From Fig. 4.11 we can see that the waist measured by the CMOS camera tends to over estimate the beam size by approximately 25 μm for beam sizes above 100 μm. More investigation is required at the lower beam sizes at which the laser is expected to operate to determine whether the increasing overestimate of the beam size is due to the intrinsic resolution of the camera or a failure in the fitting routine. It is a failure such as this which is responsible for the extreme value given by the CMOS camera at $\sigma_{\text{knife}} \approx 100$ μm.

4.5.2 Laser profiling

To measure the longitudinal profile of the laser waist, the camera was placed on a guide rail, allowing its position along the beam axis to be varied. Fifty images were taken at each of a series of locations at varying distances from the waist of the laser beam. The beam spot size at each location was then

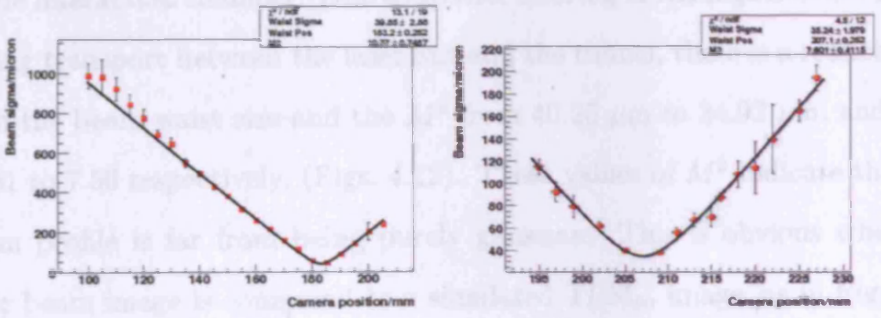

Figure 4.12: Variation of the laser beam transverse size along the beam axis. Results are shown for focusing of the beam near the aperture of the laser (left) and after transport from the hut to the PETRA tunnel (right).

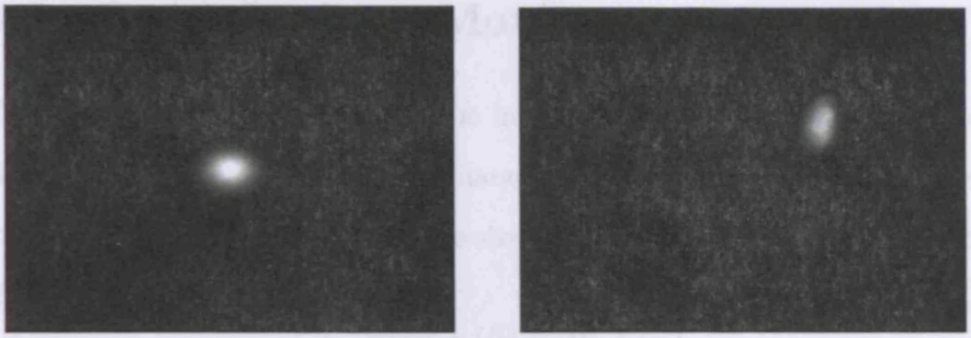

Figure 4.13: Comparison of a simulated image of a TEM_{00} mode (left) with an image of the laser beam spot (right). We see that there is much substructure to the real laser beam — this comes from higher order modes.

plotted and the results fitted to Eq. 2.12 for the beam waist spot size σ_0, the waist position z_γ and the beam quality factor M^2. The setup for this is similar to that used in the knife scans, (Fig. 4.9), only with the camera mounted on a moveable platform so that it can be moved along the laser beam axis, and without the knife edge stage.

Measurements of the longitudinal profile were made in two locations: in the laser hut (near the exit aperture of the laser), and in the beam tunnel near to the interaction chamber. Due to spatial filtering of the higher order modes during transport between the laser hut and the tunnel, there is a reduction in both the beam waist size and the M^2 from 40.25 μm to 34.92 μm, and from 10.81 to 7.56 respectively, (Figs. 4.12). These values of M^2 indicate that the beam profile is far from being purely gaussian. This is obvious when the laser beam image is compared to a simulated TEM_{00} image, as in Fig. 4.13.

4.6 Beam Position Monitor

The beam position monitor near the interaction point is composed of four pickup plates (Fig 4.14). When a charged particle bunch passes the plates, voltages U_i are induced on them, the size of which are related to the position of the bunch by:

$$x = K_x \frac{(U_1 + U_4) - (U_2 + U_3)}{U_1 + U_2 + U_3 + U_4} \tag{4.9}$$

$$y = K_y \frac{(U_1 + U_2) - (U_3 + U_4)}{U_1 + U_2 + U_3 + U_4} \tag{4.10}$$

where $K_{x/y}$ are machine constants, and U_i is the voltage in the i^{th} pickup.

The BPM serves two purposes. Firstly, it is used to position the electron beam in the interaction region — setting the beam to the last known location with good signal reduces the amount of set up time at the beginning of a run. Secondly, the output signal from the BPM is used in calibrating the trigger delays (Fig. 4.7) so that there is maximum temporal overlap between the electron bunch and the laser pulse.

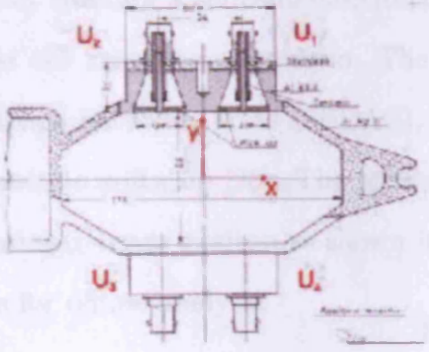

Figure 4.14: The beam position monitor pickup arragement near the laser-wire interaction point. [25]

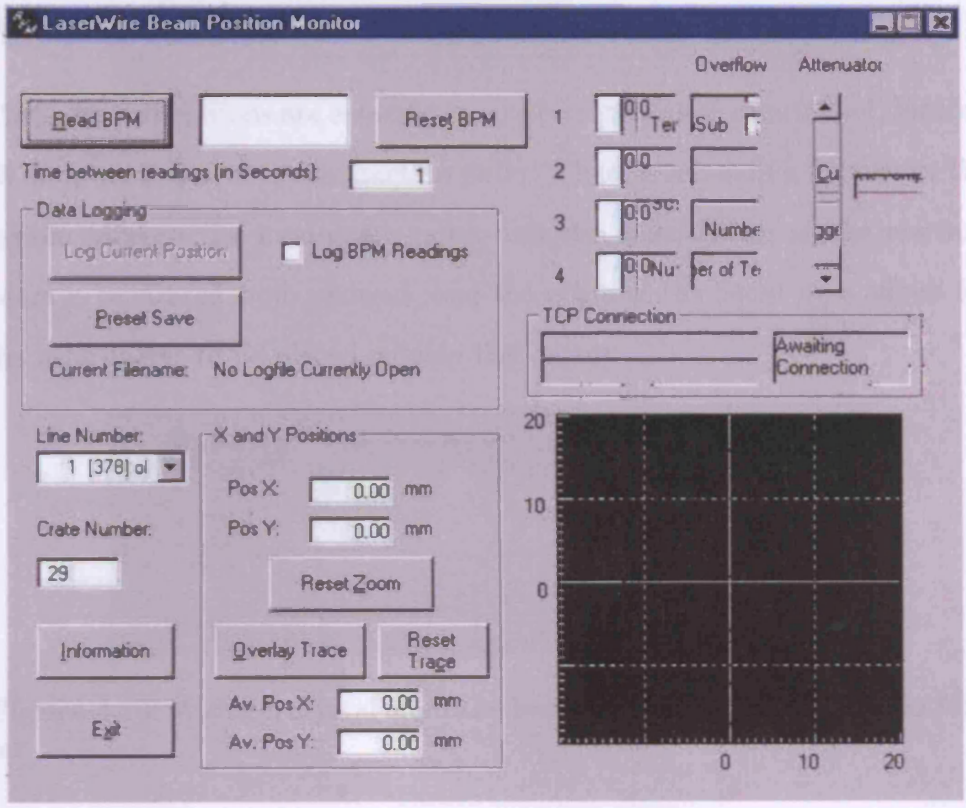

Figure 4.15: Screenshot from the BPM DAQ software.

The BPM is read out through a series of electronics to remove high frequency noise and boost the signal-to-noise ratio. The signal is then passed to a Serial Data Acquistion hardware crate (SEDAC), which relays the data to the BPM data acquisition software [26]. The software provides a graphical interface for determining beam positon as shown in Fig. 4.15, as well as writing the data to file for offline analysis.

4.7 Calorimeter

The scattered photons are detected in an electromagnetic calorimeter, located 23 m downstream of the interaction point. There is a bending magnet in the region between the interaction point and the calorimeter, so the electron beam is separated from photons, and the angle of the beam pipe allows for the calorimeter to be placed outside the vacuum.

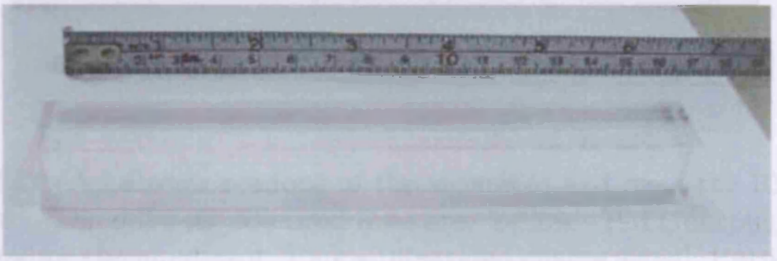

Figure 4.16: A single crystal from the lead-tungstate scintillation calorimeter.

The calorimeter is comprised of 9 blocks of lead-tungstate, $PbWO_4$, in a 3×3 matrix. Each block is a cuboid measuring $18 \times 18 \times 150$ mm. At this size, GEANT3 simulations show that the calorimeter will capture 91 % of the shower energy from a 300 MeV photon [27, 28]. The calorimeter matrix is connected to a single photomultiplier tube (PMT) - a Hamamatsu R6091 - and the whole assembly is mounted in a light-tight aluminium box.

Initially, the peak signal from the PMT was sampled directly, but any jitter in the timing of the signal with respect to the sampling window would mean that the signal would be misread. It was therefore decided to integrate the PMT signal and use this result to determine the energy deposited in the calorimeter. An integrator circuit was developd by Gary Boorman of RHUL.

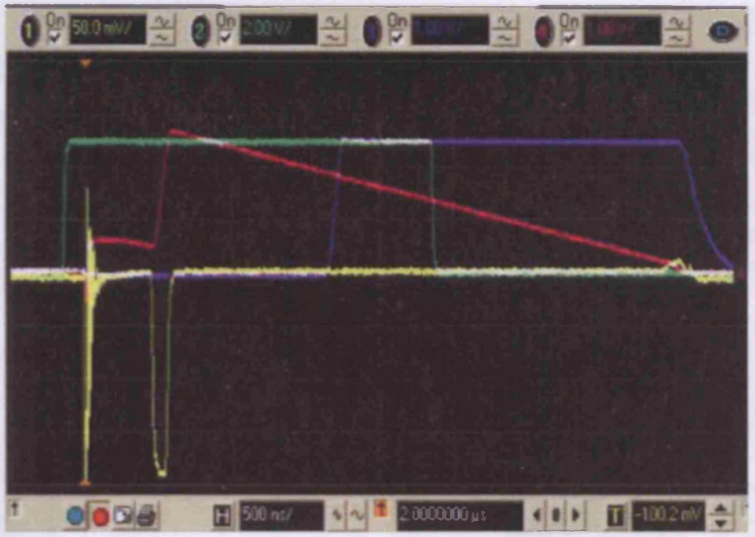

Figure 4.17: A Labview readout of the signals to and from the PMT integrator card. The different coloured lines are: Yellow - PMT output, Green - Gate signal for the integrator, Pink - Integrated charge signal, Purple - Peak integrated signal. The initial spike in the PMT output is due to crosstalk from the gate signal. It is unclear whether this is an artefact of connection to the oscilloscope during testing or whether it also occurs during full running.

Radiation Length	[mm]	8.90
Moliére Radius	[mm]	22
Density	[g/cm^3]	8.28
Avg. # Photoelectrons/MeV		16
Decay Time	[ns]	5–15

Table 4.2: Characteristics of $PbWO_4$ [29].

The signal configuration can be seen in Fig. 4.17. The PMT (integrated) voltage was read out by an ADC card, and the data passed to a DAQ program (Fig. 4.18) for graphical representation and writing to file for offline analysis.

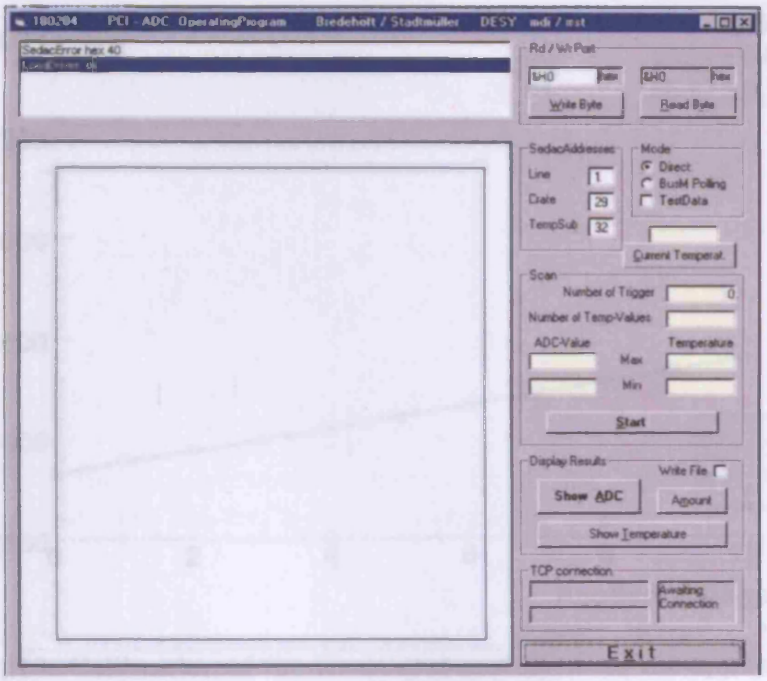

Figure 4.18: Screenshot from the calorimeter DAQ software control panel.

4.8 Beam scanning

For laserwire running, PETRA is loaded with 7 GeV electrons. The triggering for the laser is set such that the laser light will collide with the first bunch in the train, and so this bunch is filled with a higher than normal charge.

The laser beam is scanned across the electron bunch by a mirror mounted on a piezo-electric stack. A voltage of 0–10 V is amplified by a factor of 10, and applied to the stack to generate an angular deflection of 0–5 mrad. The back focal length of the focusing lens is 117 mm. A thin lens approximation shows that this generates a translation of the laser spot at the focal point of order 585 μm. The expected vertical beam size in PETRA is of order 100 μm rms, so this translation is sufficient to scan through the whole electron bunch.

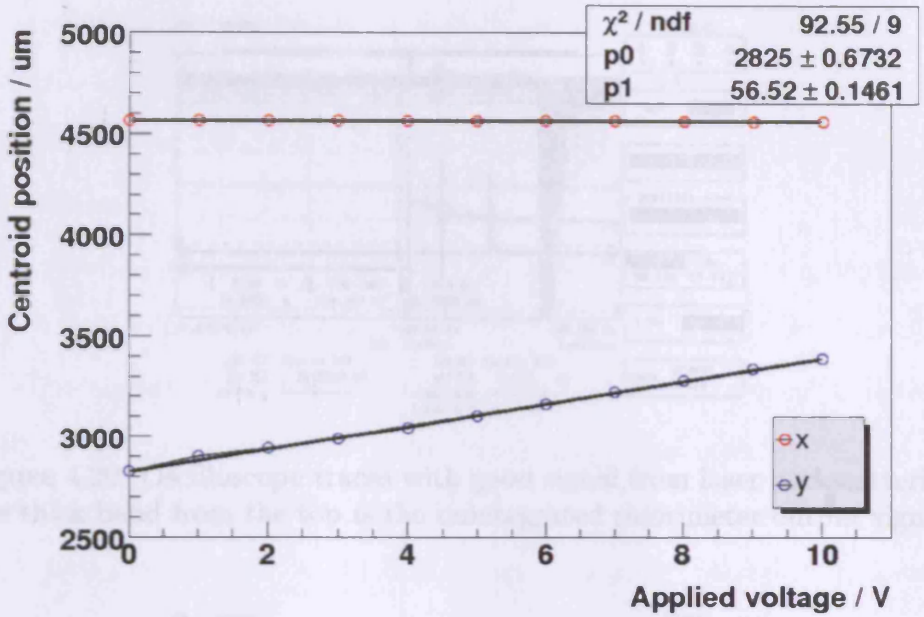

Figure 4.19: Calibration of the beam spot movement to the applied scanner voltage.

In order to verify the motion of the laser spot, the focus was re-imaged onto the chip of the camera and the centroid position measured for a sequence of voltages applied to the scanner. A simple linear fit to the resulting data points showed the actual movement of the beam spot to be 56.2 μm/V. This is shown in Fig. 4.19.

4.8.1 Slow scanning

Initial calculations from Eq. 2.9, with a crossing angle of $\alpha = \pi/2$ show that each bunch crossing should generate approximately 4200 scattered photons. However, the magnitude of the detected signal was found to be significantly lower than would be expected from this amount. This was determined by

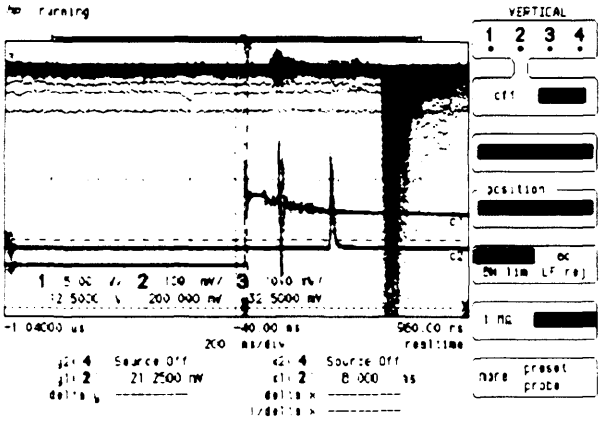

Figure 4.20: Oscilloscope traces with good signal from laser backscattering. The thick band from the top is the unintegrated calorimeter output signal.

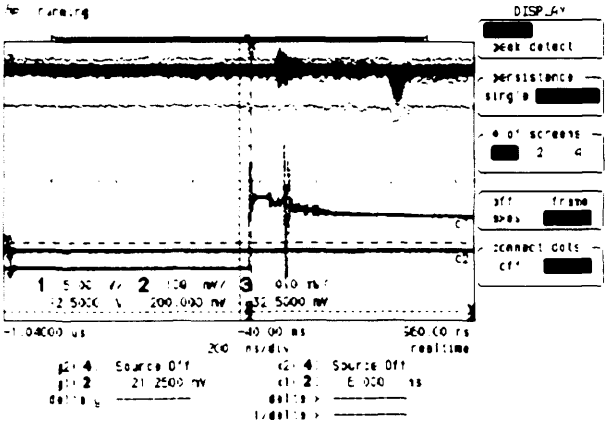

Figure 4.21: Oscilloscope traces with no signal from laser backscattering. The thick band from the top is the unintegrated calorimeter output signal. The slight peak is from synchrotron radiation backgrounds.

eye from the output signal from the calorimeter on oscilloscpe traces. An example is shown in Fig. 4.20. In this case, the thick band at the top of the trace shows the calorimeter traces for many events with good backscattering signal, while Fig. 4.21 shows the same setup with the laser switched off. As

the typical traces were much closer to those in Fig. 4.21, it was clear that a significant proportion of the signal was being lost. This motivated a full simulation of the interaction region, which is discussed briefly in Sec. 4.8.2, and in detail in [34].

In order to collect sufficient statistics it was necessary to integrate the output from a large number of bunch crossings for each position of the scanner. This meant that a full scan across the bunch could take up to 45 mins, which is clearly unacceptably slow. In a storage ring such as PETRA the beam current decreases over time which could skew the results, while in a single pass machine such as the ILC there would not be enough time to make such a measurement.

In order to determine the position of each point in the scan, the laser beam focus was re-imaged onto two cameras via beam expanders. One camera

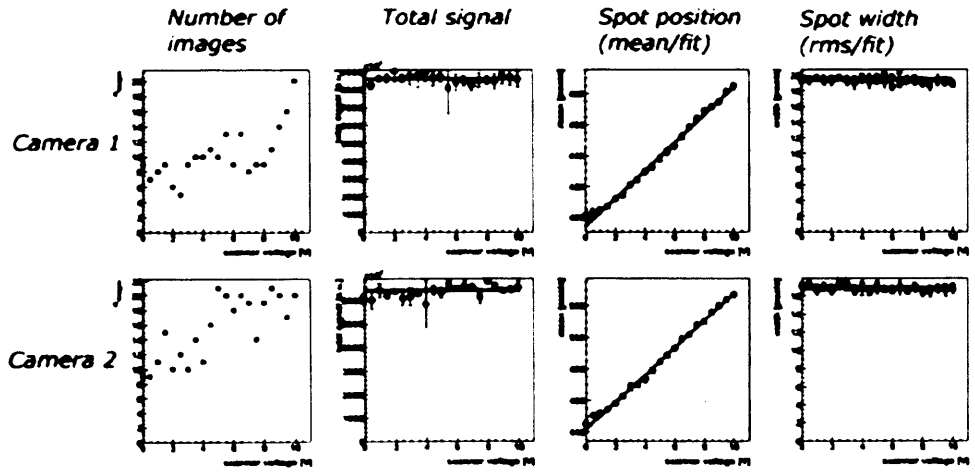

Figure 4.22: Analysis of the CCD data for the low current run, 7.1 mA. From left to right: Number of images, total intensity, spot position, and laser rms vs applied scanner voltage. [30]

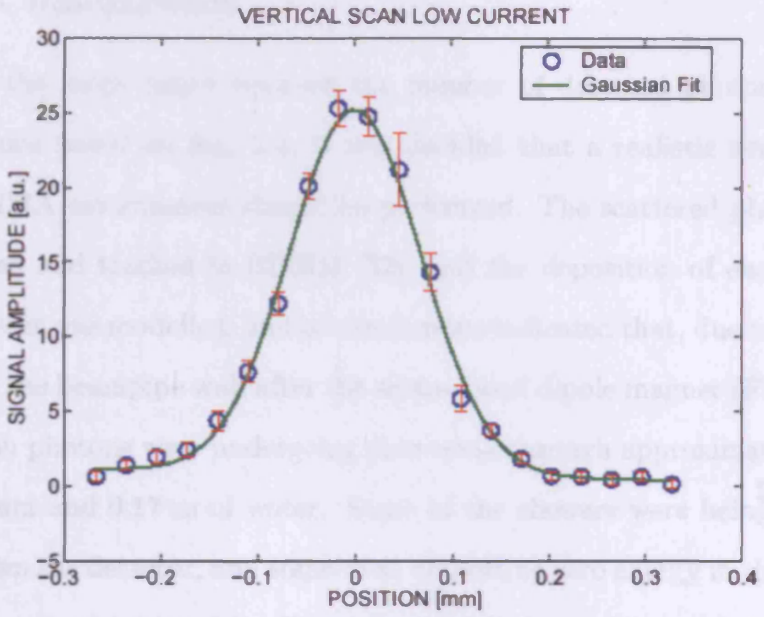

Figure 4.23: Vertical profile of the PETRA beam, taken in December 2003. In this run, the beam current was loaded to 7.1 mA, with a charge of 3.9 nC in the first bunch. This profile gives $\sigma_y = 68 \pm 3 \pm 14$ μm which is within the range of expected PETRA parameters [31].

imaged the laser light prior to the interaction point, while the other imaged the refocused light after collision with the electron beam. Collected data from the cameras is shown in Fig. 4.22. Although the cameras were not synchronised to the laser trigger, the extended time required at each scan position ensured that enough good images were captured for analysis. The mean position of the beam centroid over a number of images was measured to determine the positon, while the mean spot size at each position was reconstucted, and the mean value of this over all positions was then used to deconvolve the electron beam width from the fitted width of the signal gaussian shown in Fig. 4.23.

4.8.2 Simulations

Due to the large deficit between the number of detected photons and the predictions based on Sec. 2.4, it was decided that a realistic simulation of the PETRA environment should be performed. The scattered photons were generated and tracked in BDSIM [32], and the deposition of energy in the calorimeter was modelled. Initial simulations indicated that, due to the slight angle of the beampipe wall after the sector-bend dipole magnet (Fig. 4.4) the Compton photons were undergoing showering through approximately 1 m of aluminium and 0.17 m of water. Some of the showers were being scattered away from the detector, and some were depositing zero energy in the sensitive volume as demonstrated by Fig. 4.24. A full description of the simulation and modelling performed by John Carter of RHUL can be found in [34].

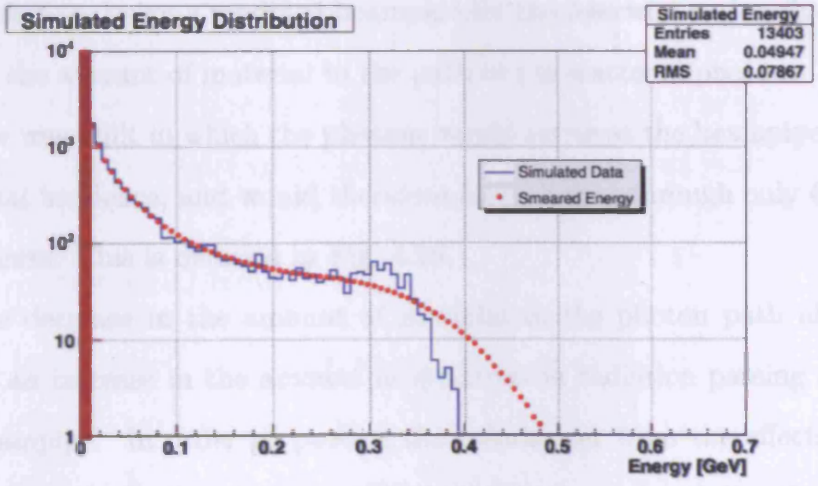

Figure 4.24: Simulated detected energy deposits in the laserwire calorimeter. Due to showering in the beampipe, 99 % of photons were not being detected (red column) [33].

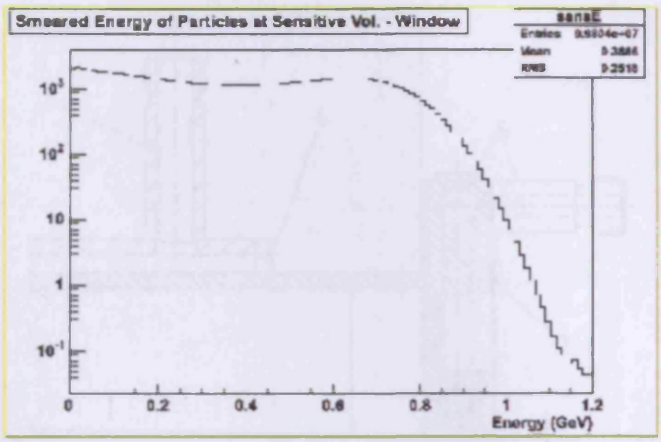

Figure 4.25: Simulated energy deposited in the laserwire calorimeter with the inclusion of an exit window [34].

4.8.3 Exit Window Installation

In order to increase the detected signal in the calorimeter, engineers at DESY were asked to design a modified beampipe for the laserwire region that would reduce the amount of material in the path of the scattered photons. An exit window was built in which the photons would arrive at the beampipe wall at a normal incidence, and would therefore have to pass through only 6 mm of aluminium. This is detailed in Fig. 4.26.

The decrease in the amount of material in the photon path also gave rise to an increase in the amount of synchrotron radiation passing through the beampipe. In order to protect the calorimeter from the effects of the increased radiation dose, 25 mm of lead shielding was placed directly in front of the detector array. This shielding was still not enough to prevent the new signal load from saturating the ADC, and so it was also necessary to reduce the gain on the PMT to allow for this. As a final consideration, the beam

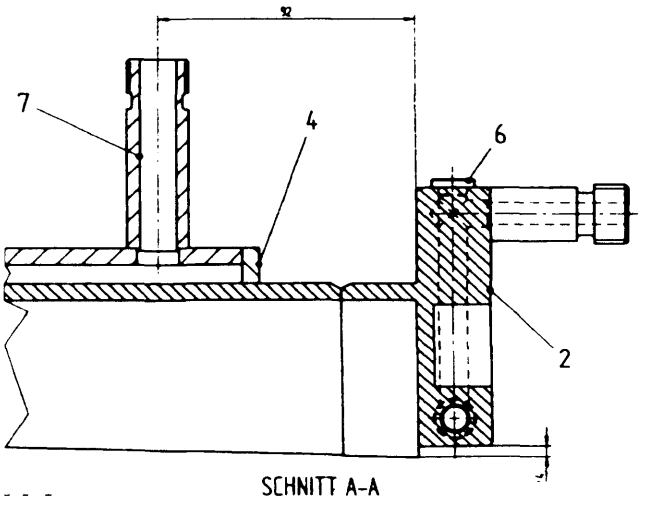

Figure 4.26: Engineering drawing of the new beampipe window for the laserwire. The aluminium window is installed perpendicular to the scattered photon trajectory. This reduces the amount of scattering in the beampipe, so a higher proportion of the signal photons reach the detector.

loading of PETRA was altered. The beam current was reduced to 1 mA and loaded entirely into the first bunch. This gave a bunch charge of $5 \cdot 10^{10}$ electrons, similar to the value in the slow-scanning case, but reduced the level of synchrotron radiation backgrounds from the unnecessary bunches.

4.8.4 Fast scanning

The increased signal meant that it was no longer necessary for the scanner to remain in a fixed position for a long time in order to collect sufficient statistics for each point in the scan. This in turn meant that the previous routine, in which each DAQ component would be switched on individually by hand within its own software framework was no longer appropriate. It became necessary to have a master control program that could initialise all

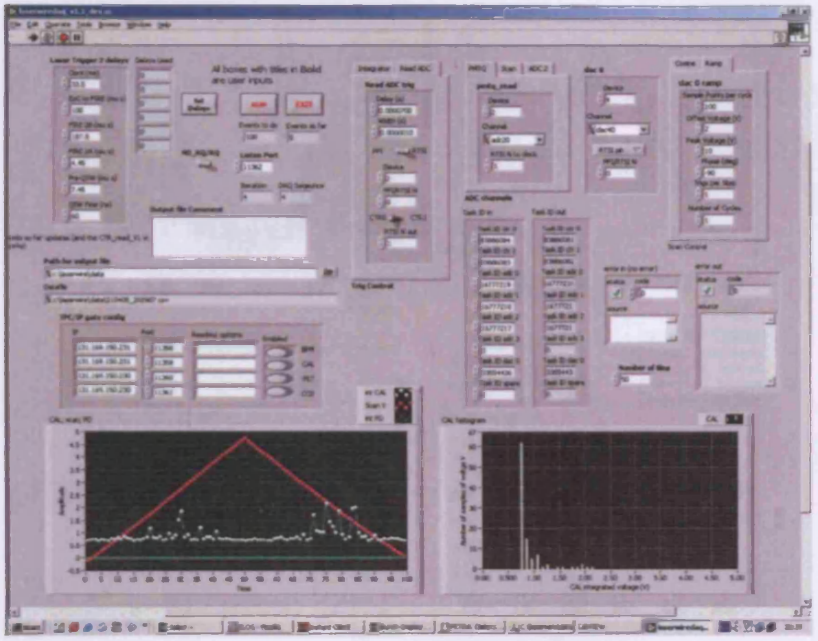

Figure 4.27: Screenshot from the laserwire DAQ master control program. This version allows control of the laser trigger delays, integrator card and scanner motion. It also contacts the selected DAQ components over TCP and receives data for display and writing to file.

the DAQ components simulataneously, ensuring that the triggering of each event was the same for each part of the system.

The software shown in Fig. 4.27 was written in LabView7 by Gary Boorman and Stewart Boogert of RHUL. It was designed to initialise the DAQ components and to send and receive data from them over TCP. It also includes a graphical display of the received data from the calorimeter, scanner and photodiode. In order to increase the efficiency of the data-taking, the DAQ for the camera system was rewritten to allow the use of a trigger signal from the laser trigger card. This ensured that every file from the camera now contained an image of the laser spot. Although the scanner is capable

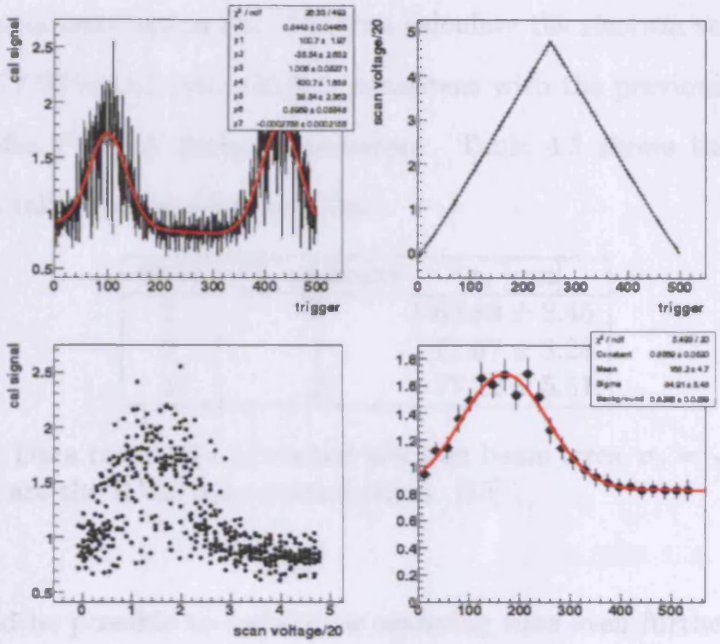

Figure 4.28: Analysis of fast scanning data. (Top left) Integrated calorimeter signal for 500 triggers. (Top right) Return scanner voltage (applied voltage/20) for the same 500 triggers. (Bottom left) Integrated calorimeter signal against the return voltage for all triggers. (Bottom right) Mean value of integrated calorimeter signal at each position, as determined by the return voltage.

of movement at a kHz rate, the laser is limited to 30 Hz, and so this became the limiting rate for scanning.

Once it was established that each bunch crossing could provide a reasonable signal level, attention moved to scanning the beam. Fig. 4.28 shows the full data set for a fast-scanning run. In this example, the applied scanner voltage was incremented from 0 to 10 V and back down again in steps of 0.2 V. Each value was maintained for five triggers. At 30 Hz, this gives a total scan time of approximately 17 s, compared with the previous time of around 45 mins. Taking the laser beam focus size for the tunnel location as

35.24 μm as determined in Sec. 4.5.2, we calculate the electron vertical beam size to be 77.25 ± 6.61 μm, which is consistent with the previous slow scans and with the PETRA design parameters. Table 4.3 shows the measured beam sizes taken during several shifts.

Shift	No. of Scans	σ_e [μm]
1	7	62.89 ± 2.45
2	7	71.67 ± 3.28
3	3	77.22 ± 5.51

Table 4.3: Data results for extracted electron beam sizes, $\sigma_e = \sqrt{\sigma_{\text{rms}}^2 - \sigma_0^2}$. The errors are the RMS from several scans. [35]

It would be possible to reduce the scanning time even further by taking fewer triggers at each position and/or taking readings at fewer positions. However, this is likely to lead to a greater uncertainty in the measured electron beam size, and so is not considered desirable. A laser which had a much higher (kHz) repetition rate would be the best method of decreasing the scan time.

4.8.5 Timing scans

The peak signal occurs when the centres of the electron bunch and the laser pulse collide. Because of the gaussian distribution of electrons along the direction of motion, adjusting the timing of the laser pulse causes a variation in the peak calorimeter signal. This variation can be used to determine the optimum timing.

The reference time used was the initial detection of signal in the BPM with respect to the firing of the laser Q-switch signal. This timing was changed by

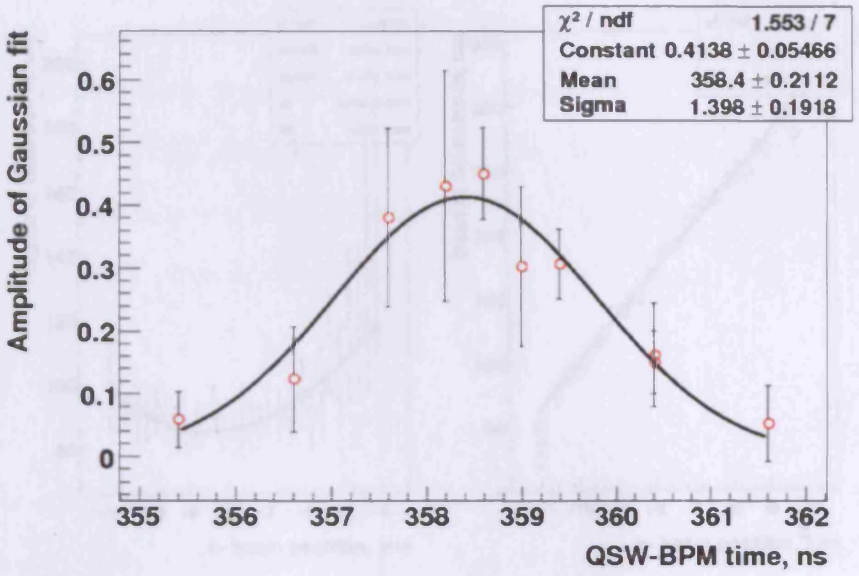

Figure 4.29: Variation in peak signal with QSW-BPM delay.

incrementally altering the delay of the Q-Switch trigger until the observed signal on the oscilloscope was seen to be significantly lower than the peak value. From a fit of the results (Fig. 4.29), it was determined that a delay of 358.4 ns produced the largest signal. However, due to the discrete nature of the registers controlling the delay, a value of 358.6 ns was the closest value which could be set.

4.8.6 Orbit bump scans

By using steering magnets to move the electron beam horizontally, it is possible to change the position along the laser beam at which the interaction occurs. For a good quality laser, the Rayleigh range for the system would mean that this positioning would not have much effect on the beam spot size over a distance of several millimetres. However, due to the poor mode

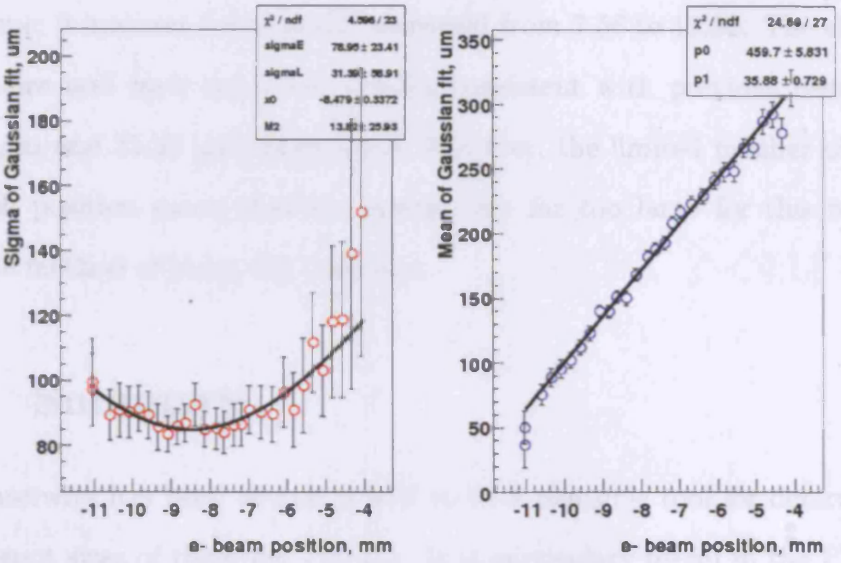

Figure 4.30: By moving the electron beam along the axis of the laser beam, the variation in the width of the laser beam allows a fit to be made to all unknown parameters (left). The mean of the fitted gaussian in Fig. 4.28 varies as the electron beam is moved. This corresponds to the laser light intersecting with the electron beam at an earlier point in the scan, as would be expected. This demonstrates that too short a focal length or too limited a scan range would not allow for a full scan of the electron beam.

quality of the actual laser, as evidenced by the high value of M^2 found in Sec. 4.5.2, the Rayleigh range was much shorter than had been hoped. To determine the effect this had upon the signal, the electron beam was moved horizontally in steps of approximately 0.2 mm over a range of around 7 mm, and the sigma of the convoluted gaussian was measured at each position, (Fig. 4.30).

Fitting the resulting distribution for $\sigma = \sqrt{\sigma_\gamma^2 + \sigma_e^2}$, where σ_γ is given by Eq. 2.12, allows a determination of M^2, σ_0, x_0 and σ_e. This measurement was taken 10 months after the profiling of the laser mentioned in Sec. 4.5.2. In

this time, it appears that the M^2 worsened from 7.56 to 13.82. The electron beam size and laser waist size remain consistent with previous results, at 78.95 μm and 31.39 μm respectively. However, the limited number of scans at each position mean that the errors were far too large for this to be a reliable method of using the laserwire.

4.9 Summary

The laserwire has been demonstrated to be a plausible tool for determining beam spot sizes of the order 100 μm. It is particulary useful in the PETRA environment, where the circulation allows each measurement to be made on the same bunch. Tests of a second laserwire in KEK, Japan, have had success in making measurements of even smaller beam sizes, down to 5 μm, although the technical challenges are much greater in this instance [36]. The recent purchase of a new laser with significantly better mode quality should allow for further testing [37]. If fast (multi-kHz) scanning can be achieved, this may be of use for emittance measurements on the same bunch in the ILC damping rings, or within a bunch train in the ILC BDS. However, the expected bunch sizes in the Interaction Region are still too small for this type of system to measure. Other laser-based devices have demonstrated measurement of beam spot sizes down to tens of nanometres [38, 39], although these are outside the scope of this thesis.

CHAPTER 5

Light Sources

X-ray light sources are used in condensed matter experiments to study the structure of matter on very small scales. The brightness of X-ray sources over the past 40 years has increased exponentially, as shown in Fig. 5.1. In this chapter we briefly the discuss the development of increasingly bright X-ray sources, and the progress towards the next generation of light sources. Finally, we introduce the Energy Recovery Linac Prototype, which is discussed in more detail in Chapter 6.

5.1 First Generation

As an electron is accelerated in the field of a bending magnet, it emits radiation over a wide spectral range, as show in Fig. 5.2. If a critical energy is defined such that 50 % of the radiated power comes from photons below this energy, we find that for electrons with an energy $E = \gamma mc^2$ and a magnet of bending radius $\rho = \frac{L_{\text{dipole}}}{\theta_{\text{dipole}}}$, where L_{dipole} is the length of the dipole and θ_{dipole} is the bending angle, the critical energy is:

$$E_{\text{crit}} = \frac{3\hbar c}{2\rho}\gamma^3 \tag{5.1}$$

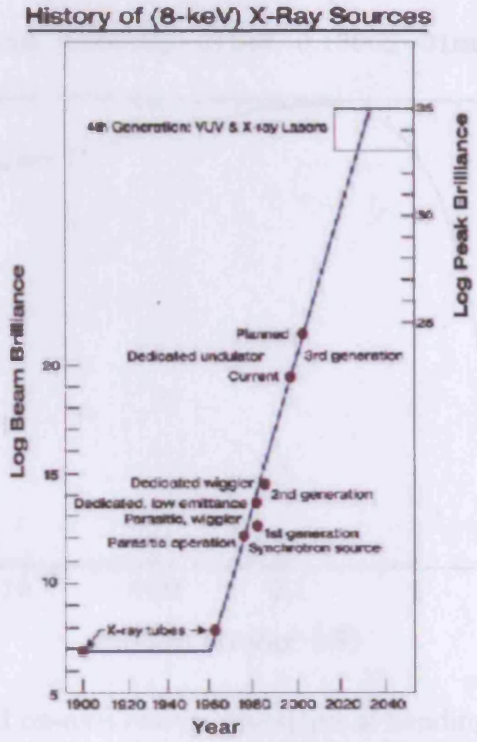

Figure 5.1: The development of 8 keV X-ray source brilliance. [40]

Photons are emitted as a fan of radiation in the bending plane and collimated within an angle of $1/\gamma$ about the tangent to the beam trajectory in the orthogonal plane. This limits the flux of available photons arriving at a detector of finite size with a fixed position relative to the beam path such that the number of synchrotron radiation photons reaching a detector of width a at a distance L from the area of emission is:

$$N_{\gamma \mathrm{SR}} = N_e \frac{5\alpha}{2\sqrt{3}} \gamma \frac{dl}{\rho} \tag{5.2}$$

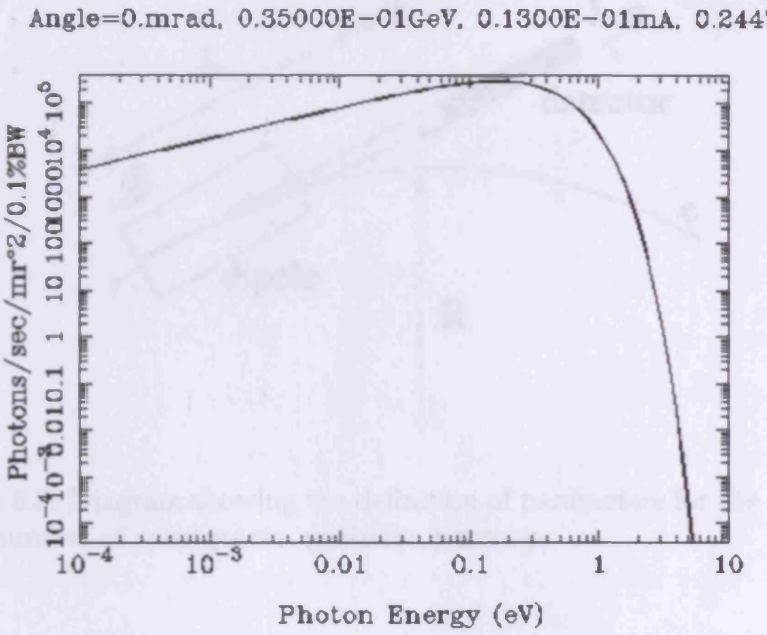

Figure 5.2: Predicted on-axis energy spectrum of bending magnet radiation from a 0.5 m dipole magnet with a field strength of 0.244 T from an electron beam with energy 35 MeV. The critical energy is 0.199 eV. [41]

where $dl = \rho\frac{a}{L}$ is the beam length over which photons emitted tangentially to the beam will enter the detector and $\alpha \approx \frac{1}{137}$ is the fine structure constant.

If we take the requirement from above that the critical energy be 30 keV for a 0.244 T bending magnet, using Eq. 5.1 we find that we require an electron energy of 13.6 GeV. This corresponds to a bending radius of 185.7 m.

5.2 Second Generation

In this instance, the electrons pass between a set of alternating magnetic poles in a "wiggler" structure. The spectral distribution remains similar

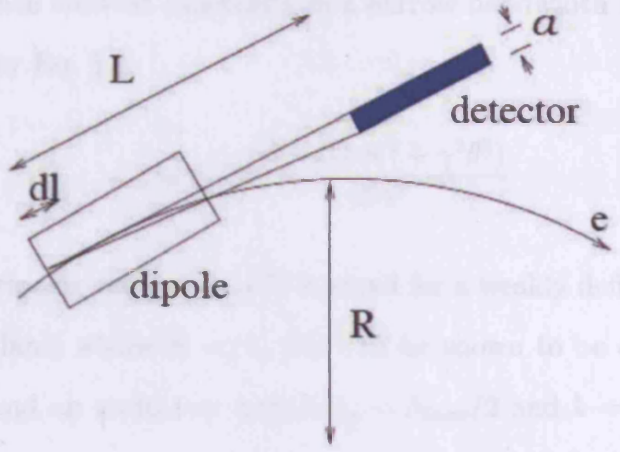

Figure 5.3: Diagram showing the definition of parameters for the calculation of the number of synchrotron radiation photons.

to that produced in a bending magnet, although the brightness increases considerably as the radiated photons are collimated about an angle $\theta_{\text{half-angle}}$ in the forward direction, given by Eq. 5.3, rather than being distributed over a large region in the bending plane.

$$\theta_{\text{half-angle}} = K/\gamma \tag{5.3}$$

In this case $K = eB_0\lambda_p/2\pi mc$ is the undulator parameter for a wiggler with period length λ_p and field strength B_0, and m is the electron mass.

5.3 Third Generation

For a weakly deflecting magnetic field, the electron motion within the wiggler is approximately sinusoidal. In this case, we have an undulator. The

radiation is then emitted coherently in a narrow bandwidth around a central value, given by Eq. 5.4.

$$\lambda_\gamma = \lambda_p \frac{(1 + 0.5K^2 + \gamma^2\theta^2)}{2i\gamma^2} \tag{5.4}$$

where i = harmonic number and K is small for a weakly deflecting magnetic field. In the limit where $K \ll 1$, this can be shown to be equal to Eq. 2.5 with $\alpha = \pi$ and an undulator period $\lambda_p = \lambda_{\text{laser}}/2$ and $k = hc/\lambda_{\text{laser}}$. That is, inverse Compton scattering acts as though the electron oscillates in an undulator field where the undulator period is half the wavelength of the incident photons. For an undulater period of 20 mm, electrons of 8 GeV are required to generate a photon energy of 30 keV.

Eq. 5.4 describes a correlation between photon energy and angle of emission. This allows us to select a chosen bandwidth by restricting the angular acceptance. For a required bandwidth $\Delta\lambda/\lambda = 1/N$, where N is the number of undulator periods, we have:

$$\theta_{\text{cen}} = \frac{K}{\gamma\sqrt{N}} \tag{5.5}$$

5.4 Free Electron Lasers

By stimulating the coherent undulator radiation into a saturation regime, lasing can be induced, hence the name Free Electron Laser (FEL). This can be achieved spontaneously in a high-gain system, where the shot-noise of the electron bunch is self-amplified by the emitted radiation, or by amplifying the

output signal using a cavity as in a conventional laser. The FLASH (formerly TTF) facility at DESY has demonstrated a peak brightness of more than 10^{28} photons s^{-1} mm^{-2} $mrad^{-2}$ 0.1% bandwidth [42]. This is approximately seven orders of magnitude greater than is achievable by a synchrotron source.

5.5 4GLS

The most desirable property of a light source is to have high average flux emission of photons. Widespread application of the electron storage ring has been the main method of attaining this — bunches of electrons are recirculated many times around the same path. This allows an average current of hundreds of milliamps. However, the beam properties are defined by the storage ring, and are dominated by the emission of synchrotron radiation that the ring is designed to deliver. Vastly improved beam properties can be achieved if the necessity for long-term beam storage can be removed.

The design of 4GLS makes use of an Energy Recovery Linac (ERL). In this case, the electrons are accelerated and circulate only once around the ring before the system recovers their energy, dumps them and replaces them with new electrons. In this way, if the beam can be injected with favourable brightness properties these can be maintained during the emission of radiation. The design for 4GLS includes FELs covering the infrared, vacuum- and extreme ultraviolet/X-ray regions of the spectrum. The VUV-FEL in the high average current loop will utilise the energy recovery system.

Potential upgrades to the 4GLS portfolio of light sources are continually being assessed, particularly where these upgrades could be easily incorpo-

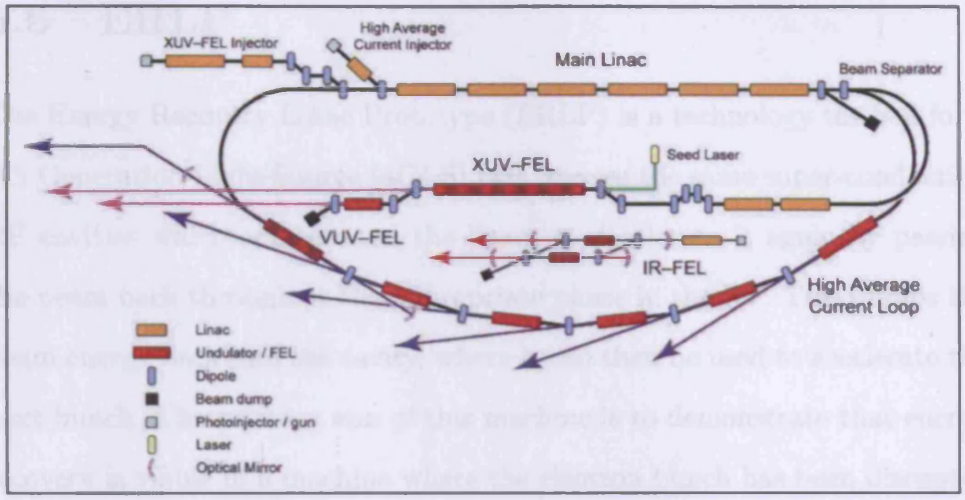

Figure 5.4: Layout of the 4GLS facility.

rated with the overall design and would improve the performance of the machine. One possiblity is that an inverse Compton scattering source could be inserted to generate X-ray pulses with femtosecond pulse lengths. This source could be inserted into the XUV-FEL line. In this case the beam energy is between 750 and 950 MeV, so in order to generate a maximum scattered photon energy of 29 keV the crossing angle α must be reduced to 5.36° at the lower energy, as shown in Eq. 2.5). The IR-FEL line is intended to run at energies between 25 and 60 MeV. This range includes the ERLP machine energy of 35 MeV. This would produce photons with the desired peak energy of 29 keV in a back-scattering geometry.

5.6 ERLP

The Energy Recovery Linac Prototype (ERLP) is a technology testbed for a 4th Generation Light Source (4GLS) [43]. It uses the same super-conducting RF cavities which acccelerated the beam to decelerate it again by passing the beam back through at the appropriate phase in the RF. This dumps the beam energy back into the cavity, where it can then be used to accelerate the next bunch. The primary aim of this machine is to demonstrate that energy recovery is viable in a machine where the electron bunch has been disrupted by passing through a wiggler to generate an Infra-Red Free Electron Laser (IR-FEL). In the future it is also expected to be used to test and demonstrate

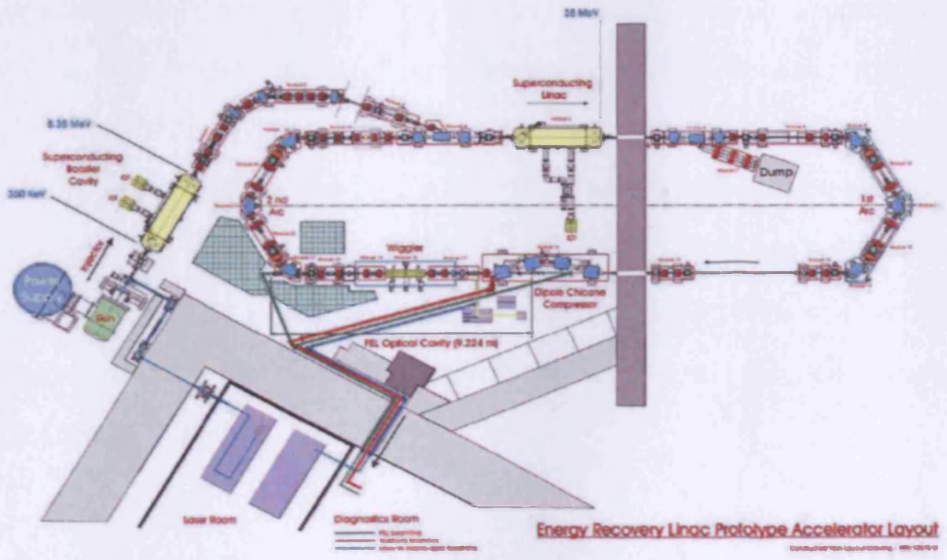

Figure 5.5: Schematic of the ERLP. The crosshatched areas are reserved for inverse Compton scattering experiments. The interaction will take place in an OTR station located just upstream of the first dipole magnet in the second arc.

other new technologies, such as the use of a helical undulator as a source of polarised positrons.

CHAPTER 6

Inverse Compton Source for ERLP

An inverse Compton source (ICS) for the ERLP could provide a brightness comparable with that of other soft X-ray sources, as well as demonstrating the feasibility of such a device for inclusion in the light source portfolio of 4GLS. The work in this chapter follows on from a preliminary exercise by M. MacDonald of Daresbury Laboratory [44]. We discuss the necessary modifications to the ERLP optical lattice that would be required to make an ICS competitive, and analyse the resulting radiation distribution to determine whether sufficient brightness can be achieved to perform condensed matter experiments.

6.1 Interaction Region

6.1.1 Requirements

Eqs. 2.13 and 2.14 show that the number of scattered photons is dependent on the convolution of the transverse sizes of the electron and laser beams, while

the temporal length of the scattered radiation pulse is clearly determined by the lengths of the laser pulse and electron bunch. To study the feasibility of both collision geometries which may be utilised in 4GLS, it is necessary for the ICS to be in a location in which both back-scattering and 90° crossing angle geometries can be satisfied. It is also required that there be some method of separating the electrons from the scattered photons, and that the bunch length be as short as possible. The solution should not require changes to the layout for standard ERLP operation, nor should it require any additional magnetic elements.

6.1.2 Proposed Solution

There is an optical transition radiation (OTR) chamber located just upstream of the return arc. This location for the ICS has numerous advantages. It would allow the drive laser to be installed in the laser room nearby, which would allow easier synchronisation and linking with other lasers in the ERLP, most notably the photo-cathode laser for the electron gun. It is positioned after the bunch compressor chicane, which allows the bunch length to be varied. It is immediately followed by a dipole magnet, (designated Ar2Dip01), which allows the electron beam to be separated from the scattered photons and also provides a route for the laser beam to be inserted. A 90° crossing angle is also feasible at this location. For this location to be used, some method of replacing or combining the OTR chamber with an interaction chamber will need to be designed. There are four quadrupoles between the OTR station and the wiggler magnet which can be used to control focusing [45]. This

location places the ICS at a position of 49.829 m along the beamline.

6.2 Beam Optics

The primary lattice for the ERLP is optimised for FEL-running and energy recovery. This provides a short electron bunch at the centre of the FEL wiggler, and delivers the bunch back to the cavities at the appropriate phase in the RF for deceleration. The beta functions of this lattice are shown Fig. 6.1. Without modification, this configuration gives an electron beam size of hundreds of microns at the suggested interaction point. The accelerator optics parameters are calculated in two separate programs: MAD8 and `elegant`. Both of these allow matching to be performed by varying the field strengths of individual magnets.

The available aperture and position for insertion of the laser beam constrains the available focus size. In order to increase the photon yield, we therefore require that the transverse size of the electron beam be made as small as possible at the interaction point.

6.2.1 MAD8

MAD8 is a tool for charged-particle optics in alternating gradient accelerators and beamlines [46]. It performs linear lattice parameter calculations, linear lattice matching, transfer matrix matching, survey calculations, closed orbit correction and particle tracking, and calculates chromatic effects and resonances, intra-beam scattering and Lie-algebraic analysis. The optical lattice of the ERLP for the FEL-mode has been optimised in MAD8 to gen-

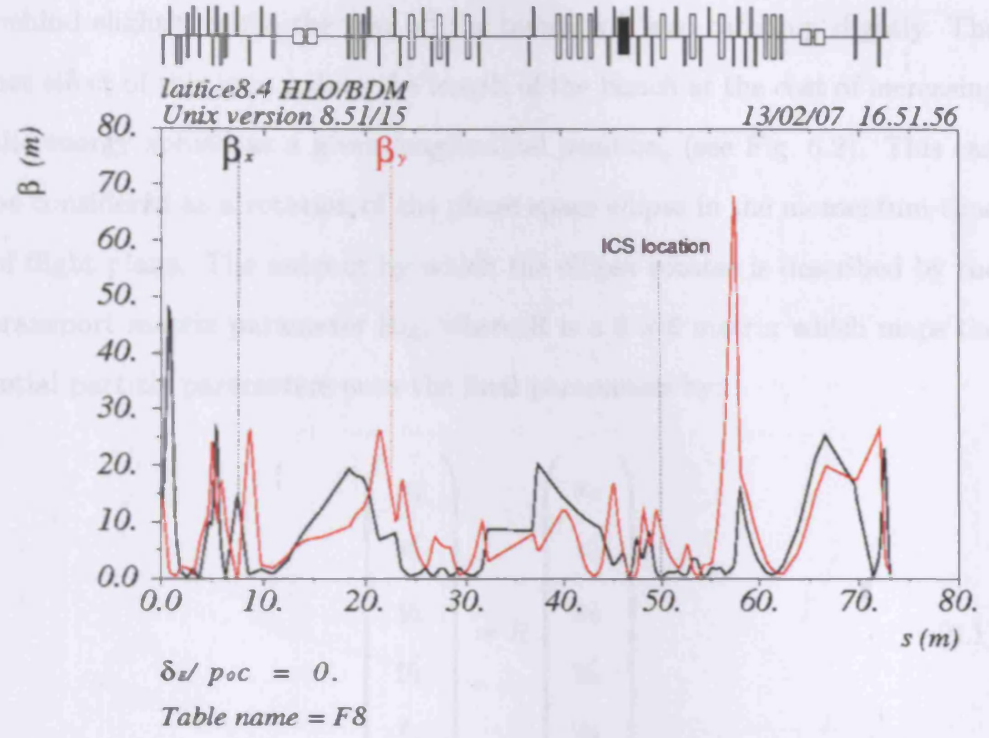

Figure 6.1: Beta functions for the ERLP in FEL-mode. These values are based on lattice 8.4.

erate a short electron bunch focused at the mid-point of the wiggler magnet. Figure 6.1 shows the beta-functions in this mode. The short bunch length is achieved by passing the bunch through a magnetic chicane. If the electron bunch is accelerated off-crest in the RF cavity, a process called chirping, then a correlation can be introduced between the longitudinal position of a particle within the bunch and its momentum. When the bunch then passes through a magnetic chicane, the higher energy particles take a shorter path than those with lower energy. If the chirp is arranged in such a fashion that the high energy particles are towards the rear of the bunch, the path difference through the chicane can be used to make the front of the bunch fall

behind slightly, while the rear off the bunch will also catch up slightly. The net effect of this is to reduce the length of the bunch at the cost of increasing the energy spread at a given longitudinal position, (see Fig. 6.2). This can be considered as a rotation of the phase space ellipse in the momentum-time of flight plane. The amount by which the ellipse rotates is described by the transport matrix parameter R_{56}, where R is a 6×6 matrix which maps the intial particle parameters onto the final parameters by:

$$\begin{pmatrix} x_1 \\ x_1' \\ y_1 \\ y_1' \\ t_1 \\ p_1 \end{pmatrix} = R \begin{pmatrix} x_0 \\ x_0' \\ y_0 \\ y_0' \\ t_0 \\ p_0 \end{pmatrix} \tag{6.1}$$

The return arc must compensate for the R_{56} of the bunch compressor chicane in order for the bunch configuration to be correct for deceleration at the RF cavities. In this mode, the beam size at the ICS interaction point is 145×784 μm. This is calculated using the beta functions shown in Fig. 6.3 and Eq. 4.6, with a normalised emittance of 5 mm mrad. The strengths of the magnets in the focusing region between the wiggler and the return arc are given in Table 6.1.

With the location of the ICS chosen to be in the OTR-station prior to Arc2, four quadrupoles are available to generate a tight electron beam focus. To obtain the maximum number of scattered photons, we require the beam

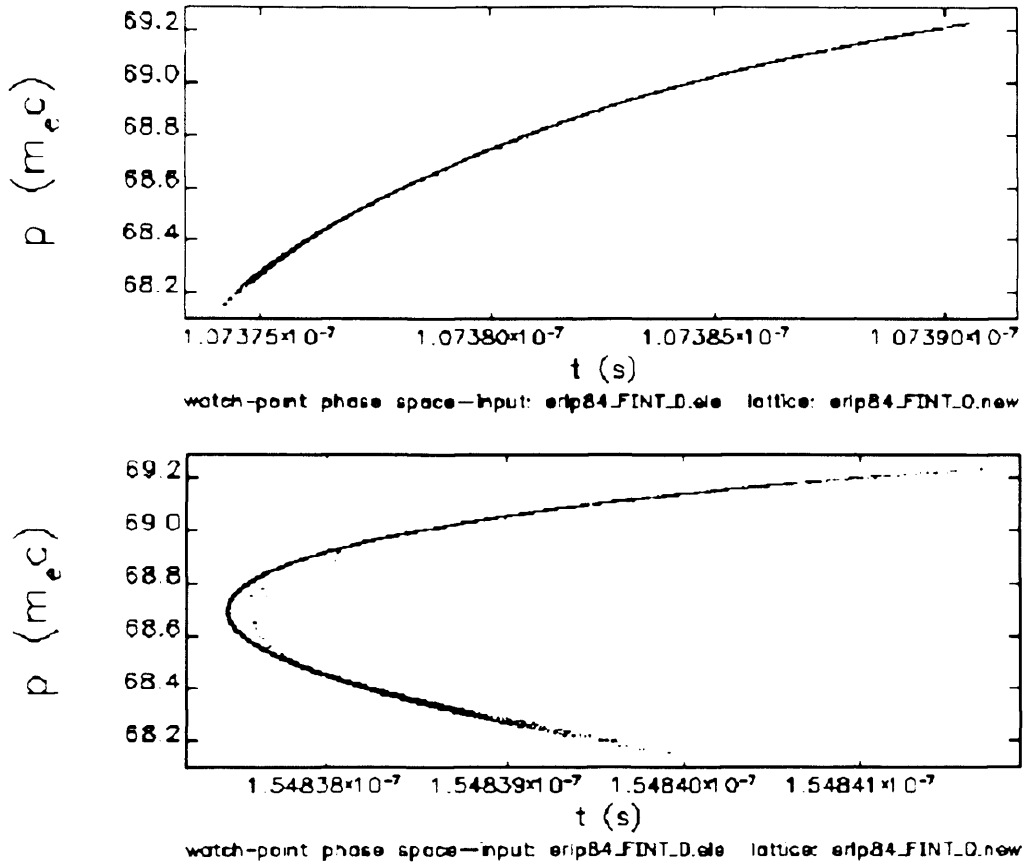

Figure 6.2: Electron beam distribution in momentum-time space before (top) and after (bottom) the bunch compressor. The magnetic chicane has $R_{56} = 0.28$.

spot size to be as small as possible. However, the specifications for the power supplies the quadrupoles are insufficient to generate focus sizes below 100×100 μm [47]. The quadrupoles themselves are recycled from Jefferson Laboratory and have rated strengths up to 4.7 T/m given appropriate power supply and cooling arrangements [45]. By allowing the strength of these quadrupoles to vary and constraining the beta- and alpha-functions of the lattice to be zero at the OTR station, *ie* requiring the beam size to be as small as possible and for a waist to be formed, we can determine the minimum

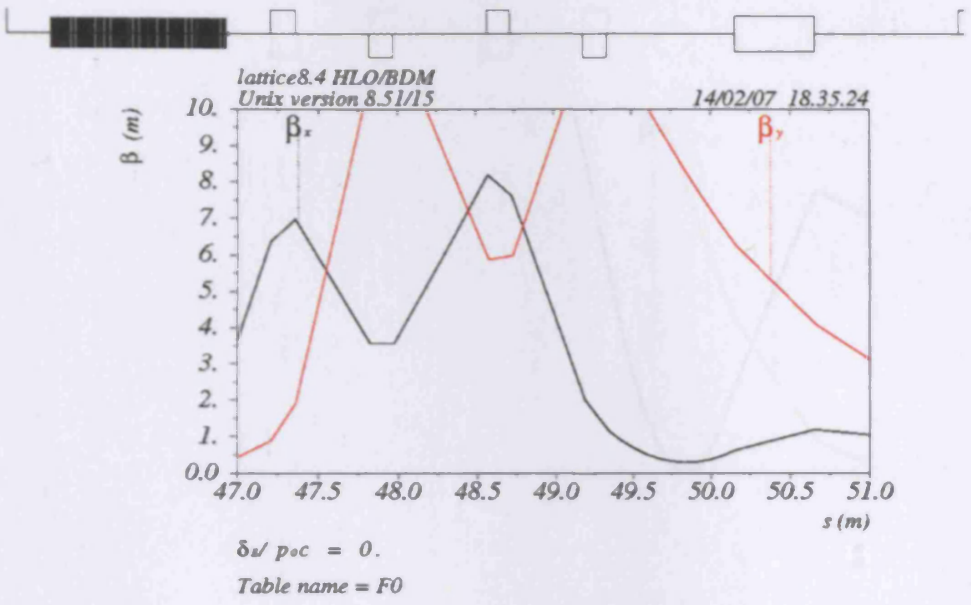

Figure 6.3: Beta functions around the ICS location in FEL-mode.

Name	Type	L [m]	Strength [m^{-2}]	Strength [T/m]	Rating [T/m]
endwig	marker	0.0			
ST3DRIFT01	drift	0.2726			
ST3QUAD01	quad	0.1524	12.0	1.40	4.7
ST3DRIFT02	drift	0.4667			
ST3QUAD02	quad	0.1524	-11.17	-1.30	4.7
ST3DRIFT03	drift	0.6003			
ST3QUAD03	quad	0.1524	10.45	1.22	4.7
ST3DRIFT04	drift	0.464			
ST3QUAD04	quad	0.1524	-6.21	0.72	4.7
ST3DRIFT05	drift	0.8088			

Table 6.1: Wiggler to Return Arc specifications for FEL-mode.

possible spot size at this location. If we also remove the constraints which apply solely to the FEL-mode, *ie* that there be a waist at the centre of the

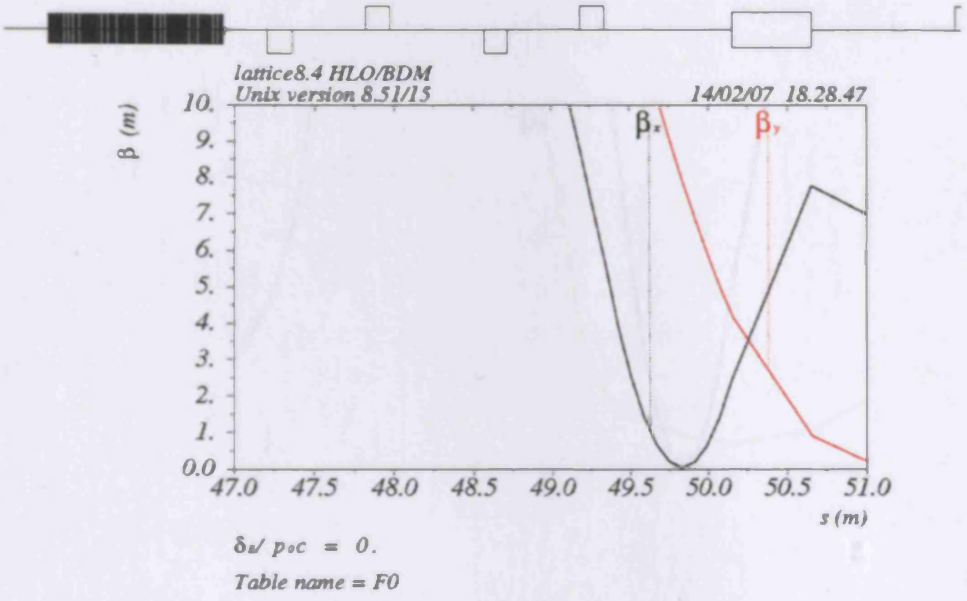

Figure 6.4: Beta functions through the ERLP in ICS-mode.

Name	Type	L [m]	Strength [m^{-2}]	Strength [T/m]	Rating [T/m]
ST3QUAD01	quad	0.1524	-2.69	-0.31	4.7
ST3QUAD02	quad	0.1524	11.05	1.29	4.7
ST3QUAD03	quad	0.1524	-9.74	-1.14	4.7
ST3QUAD04	quad	0.1524	5.41	0.63	4.7

Table 6.2: Wiggler to Return Arc specifications for ICS-mode. The drift lengths remain the same as those given in Table 6.1.

wiggler, we can achieve a spot size of 56 × 764 μm. The strengths of the magnets which are required in order to generate this configuration are given in Table 6.2 and the beta functions in the region of the ICS location are shown in Fig.6.4.

As the constraint of a focus at the centre of the wiggler has been removed,

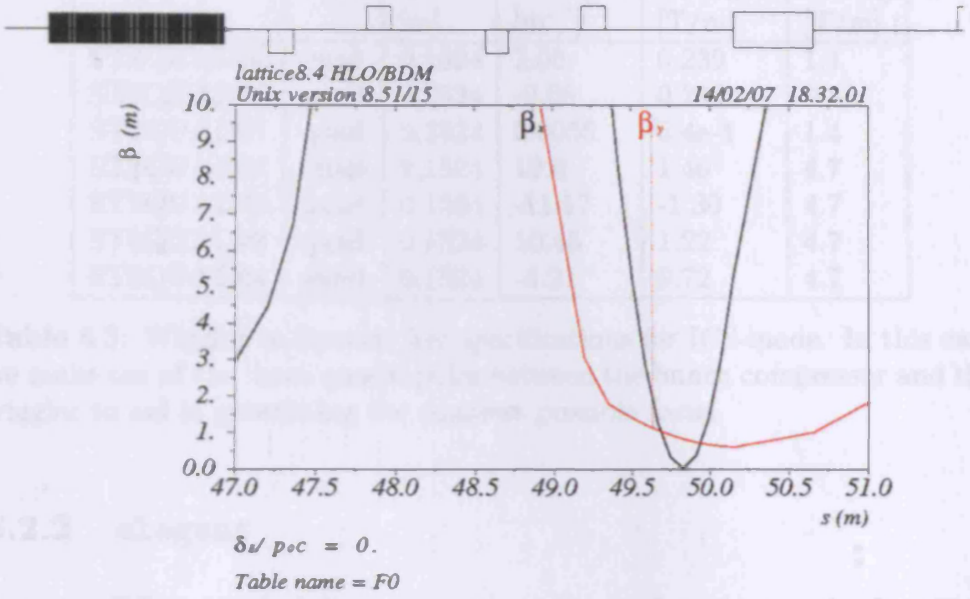

Figure 6.5: Beta functions through the ERLP in ICS-mode. In this case we make use of the three quadrupoles between the bunch compressor and the wiggler to aid in generating the smallest possible focus.

this allows the use of the three quadrupoles between the bunch compressor and the wiggler to be varied in order to generate a tighter focus. If we also remove the constraints on the beta functions prior to Ar2Dip01, which are intended to ensure passage of the beam through the return arc for energy recovery, then these extra quadrupoles can be used in conjunction with the original four to generate a beam size at the ICS location of 38.3×245 μm. The magnet strengths which generate this beam spot are described in Table 6.3, and the beta functions around the ICS location can be seen in Fig. 6.5. In this modification, it may be necessary to dump the beam in a location yet to be determined.

Name	Type	L [m]	Strength [m^{-2}]	Strength [T/m]	Rating [T/m]
ST2QUAD05	quad	0.1524	2.05	0.239	1.4
ST2QUAD06	quad	0.1524	-2.08	0.242	1.4
ST2QUAD07	quad	0.1524	0.0055	6.4e-4	1.4
ST3QUAD01	quad	0.1524	12.0	1.40	4.7
ST3QUAD02	quad	0.1524	-11.17	-1.30	4.7
ST3QUAD03	quad	0.1524	10.45	1.22	4.7
ST3QUAD04	quad	0.1524	-6.21	0.72	4.7

Table 6.3: Wiggler to Return Arc specifications for ICS-mode. In this case we make use of the three quadrupoles between the bunch compressor and the wiggler to aid in generating the smallest possible focus.

6.2.2 elegant

elegant [48] is a fully 6-D electron generation and tracking code. It utilises a modified version of the MAD input format, and can perform third order tracking of the electron distribution. While the beam spot sizes given in Sec. 6.2.1 are derived from the nominal emittance of the ERLP and the calculated beta functions from MAD8, **elegant** tracks the actual electron distribution and so gives a value for the rms beam spot sizes directly. Emittance values stated by **elegant** are also rms values.

elegant was used to track the bunch distribution through the ERLP based on the optimised lattices from MAD8. It can be seen in Fig. 6.6 that the two codes produce different beta functions based on the same optical lattice. It was therefore necessary to determine which code to continue in.

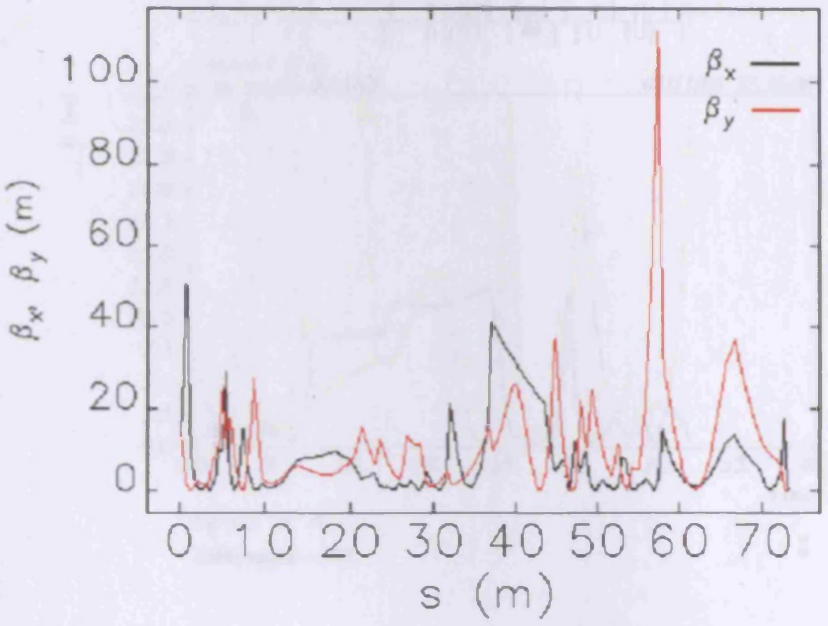

Figure 6.6: Beta functions through the ERLP in FEL-mode. These values are from lattice 8.4. It is clear that the beta functions from `elegant` differ from those calculated in MAD8 (Fig. 6.1).

6.2.3 Comparison of Tracking Codes

The most recent lattice file was arranged for MAD8, while the electron bunch input file was in the SDDS-format which is used in `elegant`. As elegant uses a variant of the MAD input format, it is a simple matter to compare the output generated by the two codes for the same lattice. Table 6.4 shows the different beta functions and beam spot sizes given by both MAD8 and `elegant` for the three lattices described in Sec. 6.2.1. We see that `elegant` calculates larger beam sizes than MAD8.

Figs. 6.7 and 6.8 demonstrate that the differences in the optics parameter calculations between MAD and `elegant` begin at accelerating elements. It

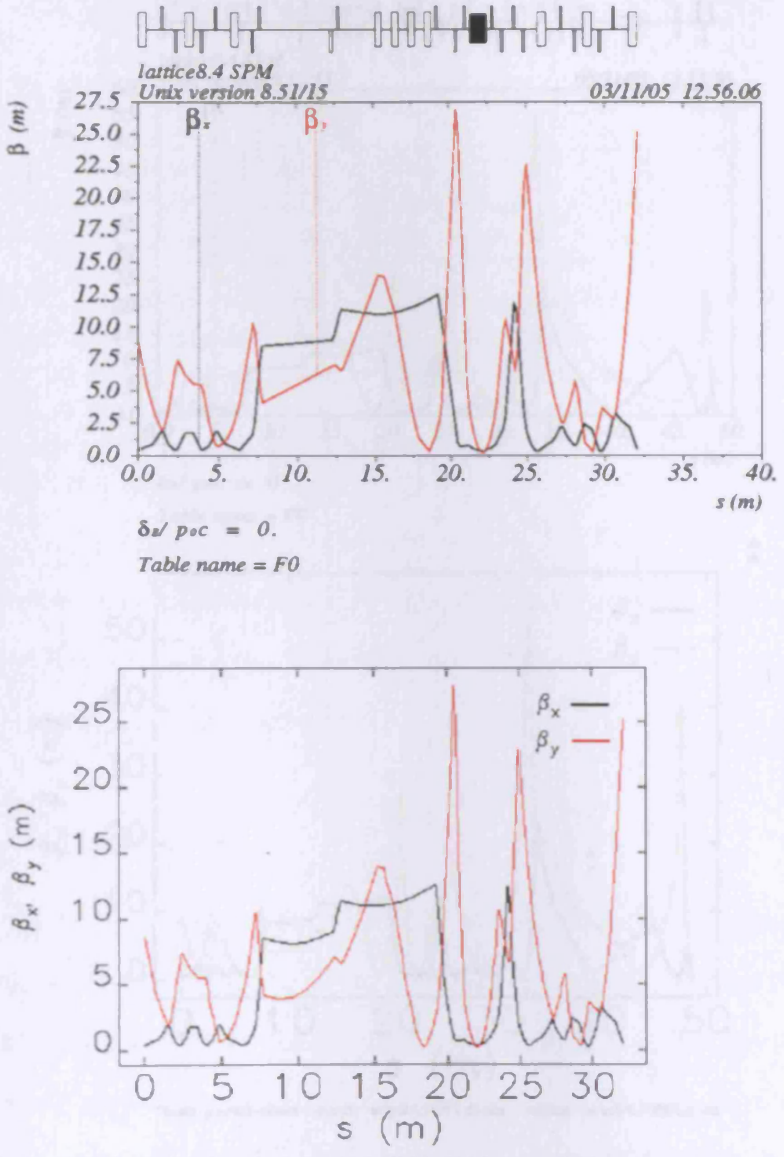

Figure 6.7: Beta functions for the ERLP from the beginning of Arc1 in MAD8 (top) and `elegant` (bottom). The final decelerating cavities are replaced with drifts of equal length. In this case we note that the beta functions are identical between the two codes.

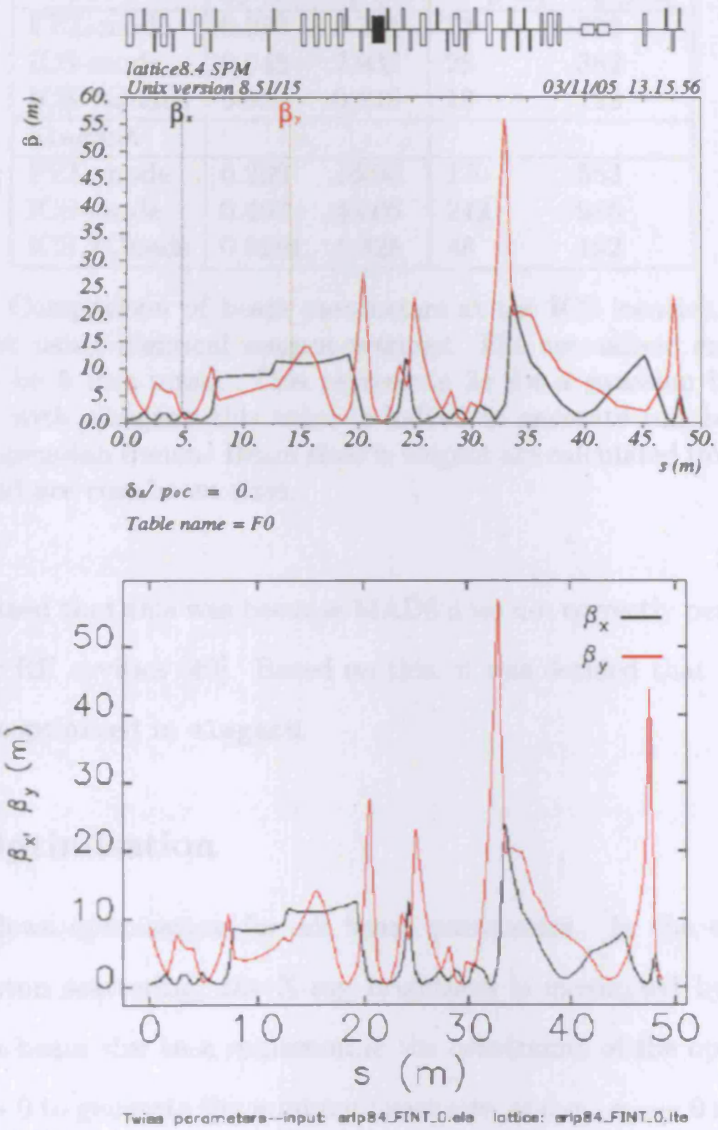

Figure 6.8: Beta functions for the ERLP from the beginning of Arc1 in MAD8 (top) and `elegant` (bottom). The final decelerating cavities are included. In this case we note that the beta functions differ between MAD8 and `elegant` only after the beginning of the cavities.

MAD8	β_x [m]	β_y [m]	σ_x [μm]	σ_y [μm]
FEL-mode	0.288	8.361	73	392
ICS-mode	0.043	7.932	28	382
ICS 7Quads	0.020	0.818	19	123
elegant				
FEL-mode	0.290	16.90	170	553
ICS-mode	0.407	43.06	242	985
ICS 7Quads	0.0291	1.328	48	192

Table 6.4: Comparison of beam parameters at the ICS location in MAD8 and **elegant** using identical magent settings. The normalised emittance is assumed to be 5 mm mrad. This represents 2σ for a gaussian beam. For comparison with **elegant** this value is halved to generate rms beam sizes, assuming a gaussian bunch. Beam sizes in elegant are calculated from particle tracking, and are rms beam sizes.

was determined that this was because MAD8 does not correctly perform end-focusing for RF cavities [49]. Based on this, it was decided that the lattice should be reoptimised in **elegant**.

6.2.4 Optimisation

elegant allows opimisation for all beam parameters. In the case of inverse Compton scattering, the X-ray brightness is maximised by reducing the electron beam size to a minimum,*ie* the constraints of the optimisation are $\sigma_x, \sigma_y \rightarrow 0$ to generate the minimum spot size, and $\alpha_x, \alpha_y \rightarrow 0$ so that the beam is at a waist. We also require that there be zero dispersion at the entrance to the return arc in order to minimise losses into Ar2Dip01 that could cause damage or backgrounds. Given that the ERLP would have to be run as a dedicated inverse Compton source, some thought was given to whether the wiggler magnet could be removed and replaced with a section of beam

σ_x [μm]	σ_y [μm]	Waist position [m]	Wiggler?
27.03	7.12	0.32352	n
21.59	13.41	0.08088	n
24.43	15.16	0.32352	n
13.45	19.81	0.32352	y
17.55	22.00	0.08088	n
16.17	27.10	0.32352	n
16.23	27.10	0.32352	n
14.06	31.29	0.32352	y

Table 6.5: Minimised electron beam sizes from `elegant`, along with the distance of the optimised focus from the end of the final focusing quadrupole, and whether the wiggler magnet was included. The OTR station is located at 0.32352 m.

pipe. This would further reduce the constraints in the region immediately upstream of the ICS location. As an exercise to determine the minimum possible electron beam spot size, the waist position of the electron beam was permitted to vary between the end of the final focusing quadrupole and the beginning of the bending magnet. The resulting beam sizes are shown in Table 6.5.

As can be seen, it was found to be possible to achieve a small electron focus size while still including the wiggler magnet. In both of these cases, the focus is located at the position of the OTR chamber, and so it was decided that the wiggler should remain. The final optics are then chosen by which remaining lattice produces the smallest focus. This gave a final electron beam focus spot size of $\sigma_x = 13.45$ μm and $\sigma_y = 19.81$ μm. The results of this optimisation are shown in Fig. 6.9. The beta functions in the region of the ICS location are shown in Fig. 6.10.

Optimisation of the beam line downstream of the interaction point has

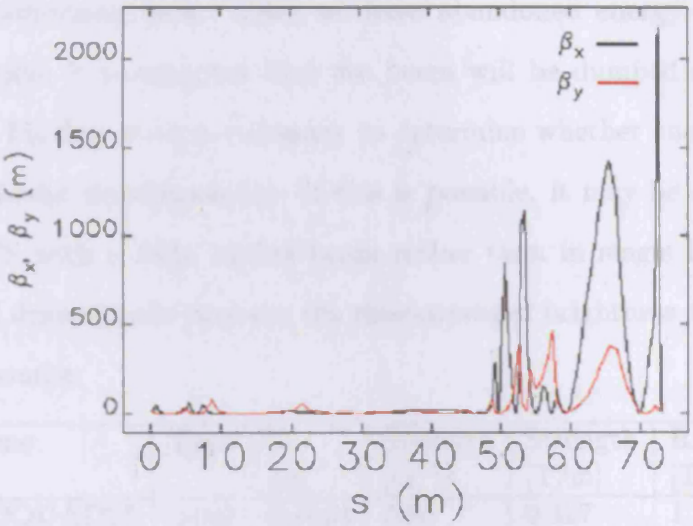

Figure 6.9: Beta functions for the optimised ICS lattice from `elegant`, using the seven quadrupoles described in Table 6.6.

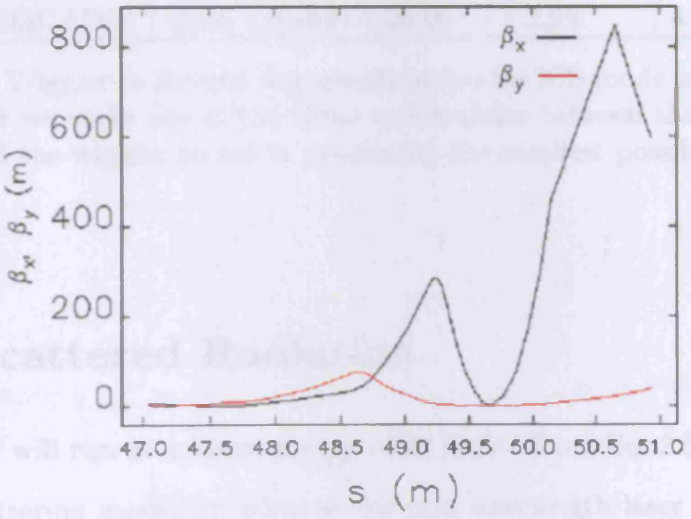

Figure 6.10: Beta functions for the optimised ICS lattice from `elegant` in the region of the ICS location, using the seven quadrupoles described in Table 6.6.

not been performed here. Since we have abandoned energy recovery for the ICS mode, it is expected that the beam will be dumped shortly after Ar2Dip01. Further work is necessary to determine whether energy recovery can be achieved simultaneously. If this is possible, it may be an option to run the ICS with a fully loaded beam rather than in single bunch mode. This would dramatically increase the time-averaged brightness of the inverse Compton source.

Name	Type	L [m]	Strength [m^{-2}]	Strength [T/m]	Rating [T/m]
ST2QUAD05	quad	0.1524	2.80	0.327	1.4
ST2QUAD06	quad	0.1524	-9.30	-1.09	1.4
ST2QUAD07	quad	0.1524	12.0	1.40	1.4
ST3QUAD01	quad	0.1524	20.56	2.40	4.7
ST3QUAD02	quad	0.1524	5.05	0.589	4.7
ST3QUAD03	quad	0.1524	-14.57	-1.70	4.7
ST3QUAD04	quad	0.1524	25.66	2.99	4.7

Table 6.6: Wiggler to Return Arc specifications for ICS-mode from `elegant`. In this case we make use of the three quadrupoles between the bunch compressor and the wiggler to aid in generating the smallest possible focus.

6.3 Scattered Radiation

The ERLP will run at a beam energy of 35 MeV. From Eq. 2.5, we see that a back-scattering geometry using an 800 nm wavelength laser will generate photons with a peak energy of approximately 29 keV, and from Fig. 2.3 we see that scattered photons within a cone of half-opening angle of $1/2\gamma$ will have an energy bandwidth of approximately 14 %.

6.3.1 Photon Flux

Having minimised the electron beam size at the ICS location, it becomes necessary to match the laser beam spot size to this in order to maximise the flux of scattered photons. From Eq. 2.13 we find that the flux is inversely proportional to the laser beam waist size. However, this equation does not take account of the variation in the laser spot size along the beam axis. Fig. 6.11 shows the results of a full numerical solution to the overlap integral in Eq 2.9 for the electron beam configurations generated in Sec. 6.2.4. The resulting number of photons scattered from a laser focus of 20 μm rms by each of these beam configuratons is given in Table 6.9.

Applying a rotation to the electron beam, we can also account for the effect of the crossing angle on the photon flux. In order to make the full description of the system as simple as possible, we fix the laser beam to be travelling along the z-axis and rotate the frame of reference of the electron

Bunch charge	80 pC
Electron Energy	35 MeV
Normalised emittance	5 mm mrad
Electron Energy Spread	0.2 %
Bunch length (rms)	300 fs

Table 6.7: Parameters of the electron beam in the ERLP.

Pulse energy	0.8 J
Pulse length	200 fs
Wavelength	800 nm
Quality factor (M^2)	< 1.5

Table 6.8: Parameters of the laser beam which provides the incident photons for inverse Compton scattering.

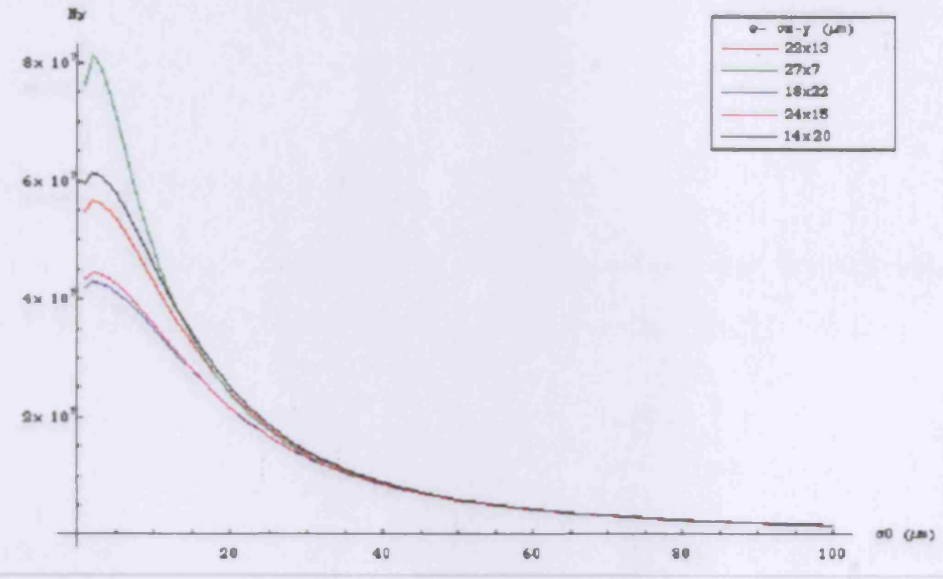

Figure 6.11: Full numerical calculations of the number of scattered X-ray photons per bunch crossing as a function of the laser focal spot size. σ_0. Several different electron beam geometries are plotted. Electron and laser beam properties are given in Tables 6.7 and 6.8 respectively.

Electron beam σ_x (μm)	Electron beam σ_y (μm)	N_γ (10^7)
21.6	13.4	2.39
27.0	7.1	2.37
17.6	22.0	2.14
24.4	15.2	2.14
13.5	19.8	2.50

Table 6.9: Achievable electron beam sizes at the interaction point and the corresponding photon production from a 20 μm rms laser spot.

beam, ie: $\rho_e(x, y, z, t) \rightarrow \rho_e(x', y, z', t)$ where:

$$\begin{pmatrix} x' \\ z' \end{pmatrix} = \begin{pmatrix} \cos\alpha & \sin\alpha \\ -\sin\alpha & \cos\alpha \end{pmatrix} \begin{pmatrix} x \\ z \end{pmatrix} \tag{6.2}$$

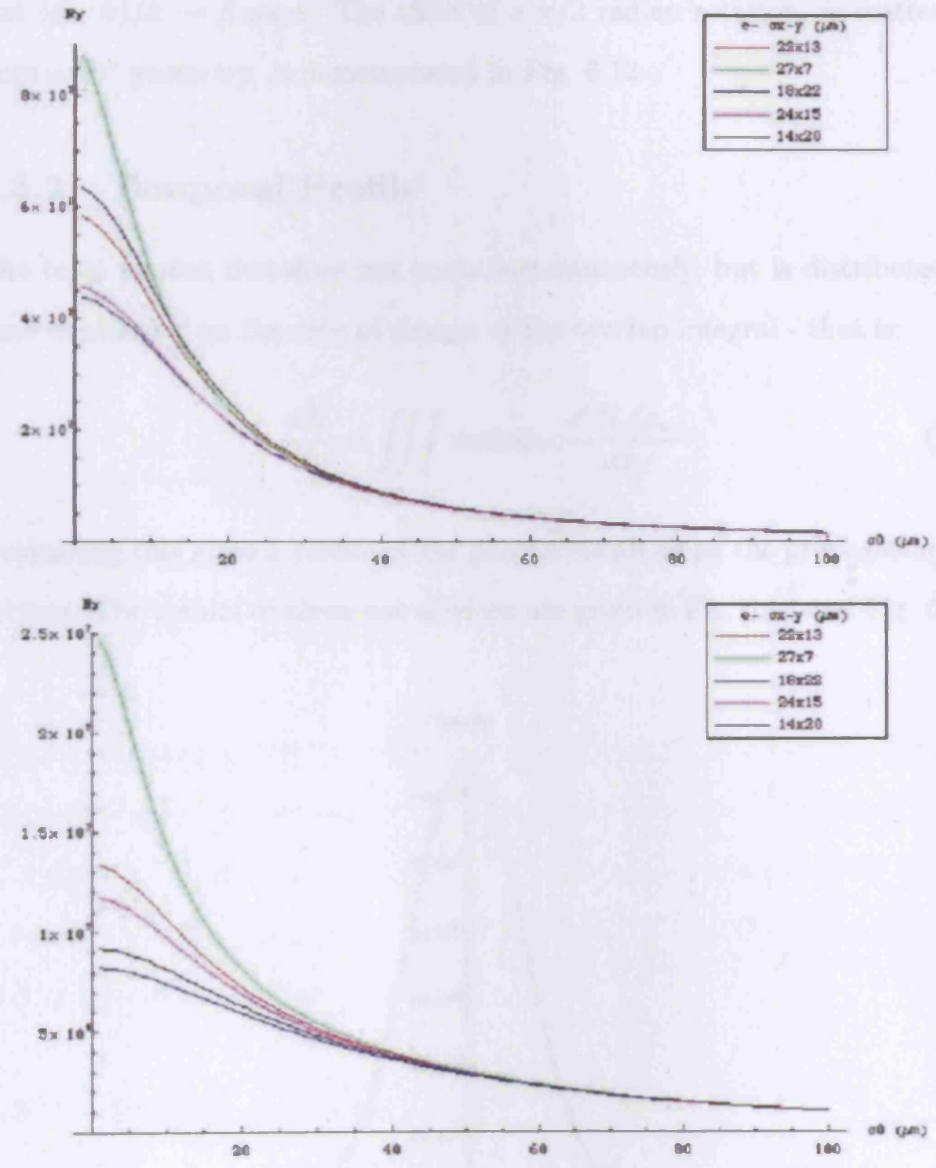

Figure 6.12: The same calculations from Fig. 6.11 are applied with σ_γ held constant as described above. We notice that the functional form remains close to that of the full calculation above a laser beam spot size of a few microns. Results are shown for (top) back-scattering $\alpha = \pi$ and (bottom) side-scattering $\alpha = \pi/2$ geometries.

and $(\boldsymbol{\beta} \cdot \boldsymbol{k})/k \rightarrow \beta \cos\alpha$. The effect of a $\pi/2$ radian rotation, *ie* scattering from a 90° geometry, is demonstrated in Fig. 6.12.

6.3.2 Temporal Profile

The total photon flux does not occur instantaneously, but is distributed in time depending on the rate of change of the overlap integral - that is:

$$\frac{dN}{dt} = \iiint dx dr dz \, c \frac{d^4 N_\gamma(x_\nu)}{dx_\nu} \tag{6.3}$$

Evaluating this gives a profile of the photon bunch along the propagating direction. The results of these calculations are given in Fig. 6.13 and Fig. 6.14.

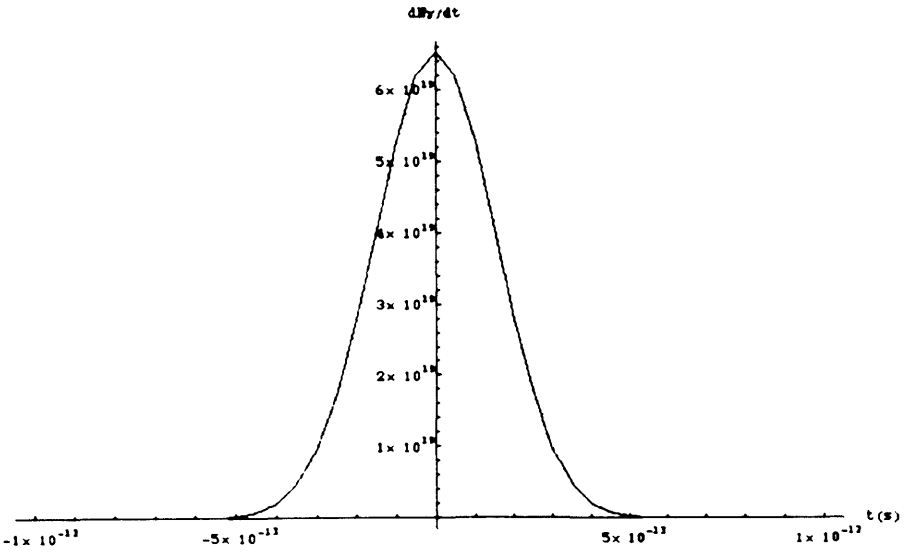

Figure 6.13: X-ray production rate (photons s^{-1}) as a function of time. For beam parameters from Tables 6.7 and 6.8, the rms pulse length of the X-rays is 153 fs for a back-scattering geometry.

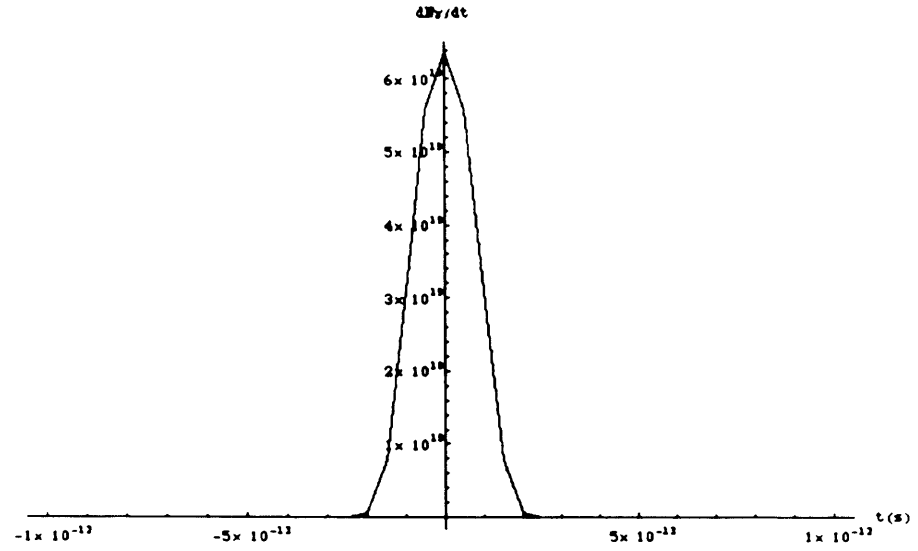

Figure 6.14: X-ray production rate (photons s^{-1}) as a function of time. For beam parameters from Tables 6.7 and 6.8, the rms pulse length of the X-rays is 78 fs for a 90° crossing angle.

As a complementary light source for 4GLS, the ERLP X-ray source must maintain the features that a 4GLS light source requires. The major point of these is ultra-short pulse lengths. This is amply demonstrated by the ICS, with pulse lengths show here of between 78 and 153 fs for 90° and back-scattering geometries respectively.

6.3.3 Effects of Jitter

Throughout the above, it has been assumed that the electron and photon bunches have been interacting at the time and position required to generate maximum X-ray flux, *ie* $(x, y, z)_{e,\gamma} = 0$. Figs. 6.15 and 6.16 show the effects of beam misalignments in the cases of back-scattering and 90° crossing angles respectively. It is clear that small deviations in the position of the

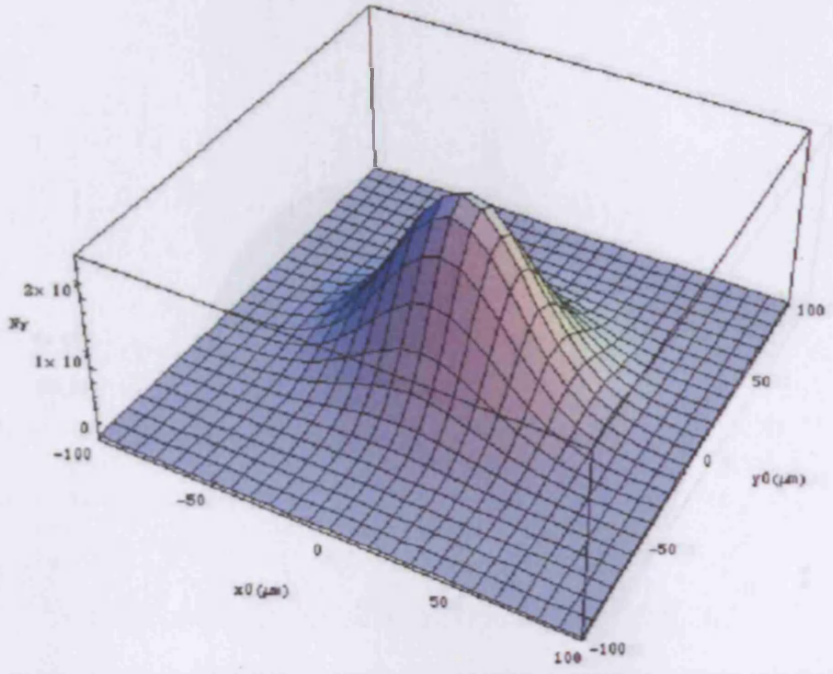

Figure 6.15: Effect of beam misalignments on the total photon scattering rate. Here we have used an electron beam with $\sigma_x = 13.45\ \mu$m, $\sigma_y = 19.81\ \mu$m and a laser beam with $\sigma_0 = 20\ \mu$m in a backscattering geometry. x_0 and y_0 are the distances between the beam centres, *ie* $x_0 = x_e - x_\gamma$.

electron and laser beams can cause large reductions in the flux of scattered photons. There have not yet been any in depth studies of jitter in the ERLP, although the specifications which have been required for the drive laser state a timing jitter of less than 400 ps. If we assume as a general rule that the rms spatial jitter of both beams is to be equal to the rms size of the beam in each direction, we can then determine the effects of this on the total X-ray production in both back- and side-scattering geometries[1]. From Eq. 2.13 we see that, for a back-scattering geometry, the X-ray production falls off as a

[1] We do not look specifically at the top-scattering geometry, as this is a trivial $x, y \leftrightarrow y, x$ transformation on the laser beam.

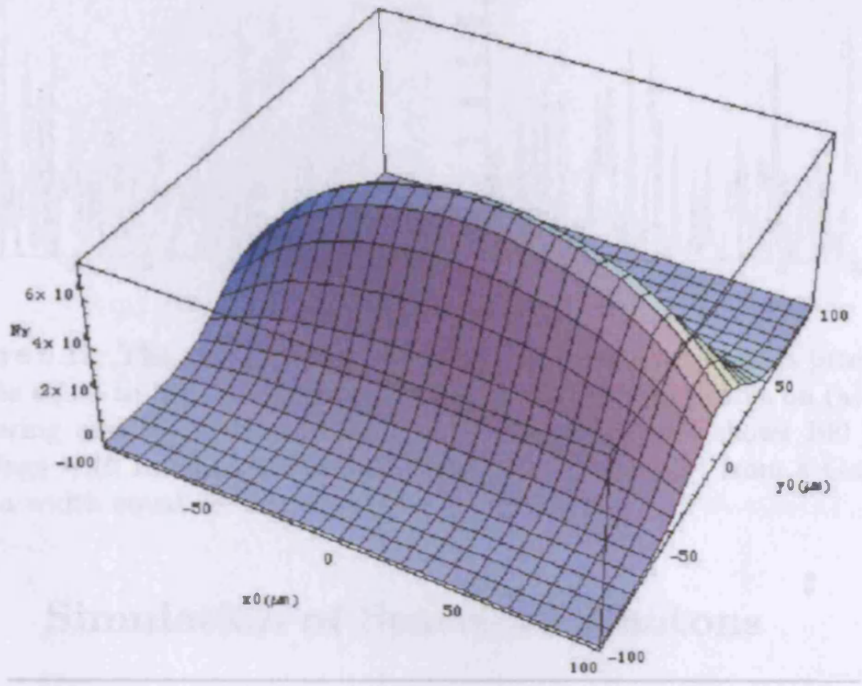

Figure 6.16: Effect of beam misalignments on the total photon scattering rate. Here we have used an electron beam with $\sigma_x = 13.45\ \mu$m, $\sigma_y = 19.81\ \mu$m and a laser beam with $\sigma_0 = 20\ \mu$m in a side-scattering geometry.

Gaussian dependent on the separation of the bunch centres in x and y.

Fig. 6.17 shows the importance of minimizing jitter — with spatial jitter which has an rms equal to the beam spot size, the mean number of scattered photons per bunch crossing is reduced to only 29 % of the peak value in the back-scattering geometry, and as low as 9 % for a 90° crossing angle. Timing jitter is particularly detrimental in the case of side-scattering due to the short electron bunches and laser pulses.

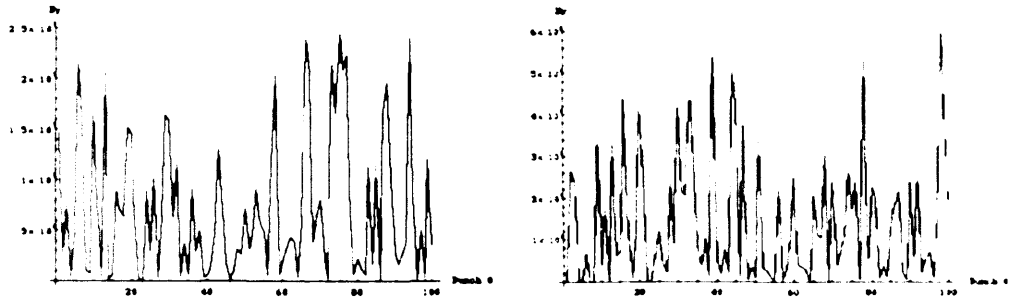

(a) (b)

Figure 6.17: The effects of rms 400 ps timing jitter and position jitter with an rms equal to the beam spot size in all planes on both beams on (a) back-scattering and (b) side-scattering geometries. Each plot shows 100 bunch crossings with random spatial and timing offsets sampled from a Gaussian with a width equal to the relevant beam size.

6.4 Simulation of Scattered Photons

The correlation between the scattered X-ray energy and angle of emission is based on a fixed trajectory for the incident photon and electron. However, in a bunch of $5 \cdot 10^8$ particles, there is a distribution in positions and angles. This contributes to a spread in the scattered photons' energies. There are three major contributions to this energy spread:

$$\frac{\Delta k'}{k'} = \frac{\Delta k}{k} \quad \text{Laser bandwidth} \tag{6.4}$$

$$2\frac{\Delta \gamma}{\gamma} \quad \text{Electron energy spread} \tag{6.5}$$

$$\frac{\gamma^2}{2}(\Delta x')^2 \quad \text{Electron divergence} \tag{6.6}$$

In the case where the laser focal spot is greater than 10μm the laser divergence does not contribute significantly to the X-ray energy spread. From

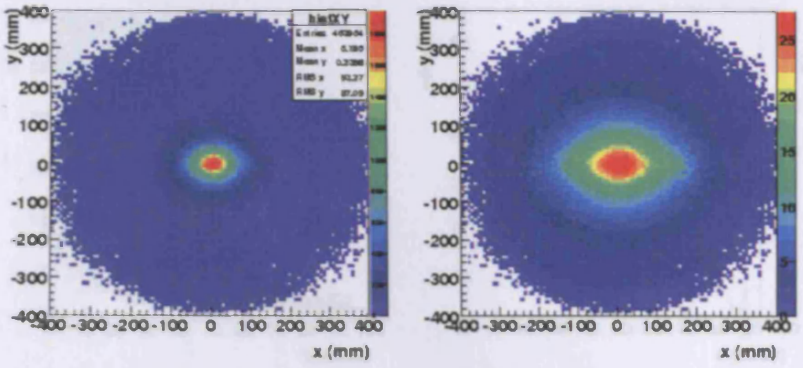

(a) Spatial distribution for ~$5 \cdot 10^5$ photons.

(b) Mean energy in keV of photons in each 8×8 mm bin of (a).

Figure 6.18: The distribution of photons and their mean energies at a plane 5 m from the interaction point.

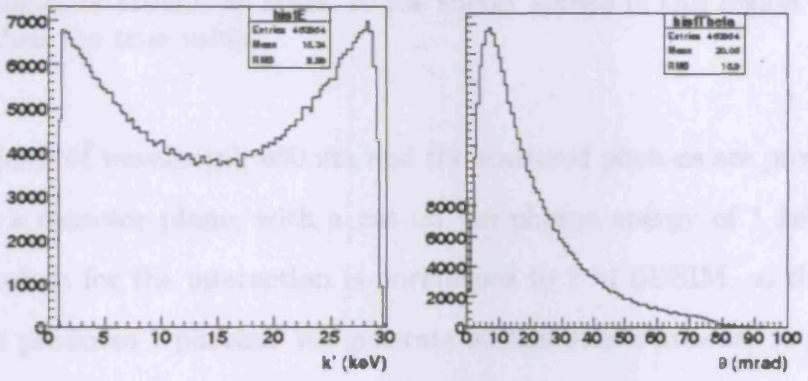

(a) Photon energy distribution. cf Fig. 2.4.

(b) Photon angular distribution. cf Fig. 2.3.

Figure 6.19: Distribution of scattered photon energies and angles from BDSIM.

Table 6.9, we see that an electron beam size of 13.5 μm $\times$ 19.8 μm produces the highest photon count from a laser with a 20 μm rms focus. The electron bunch profile at the interaction point is then taken from `elegant` and converted for use in BDSIM. In BDSIM, the bunch is then simulated interacting

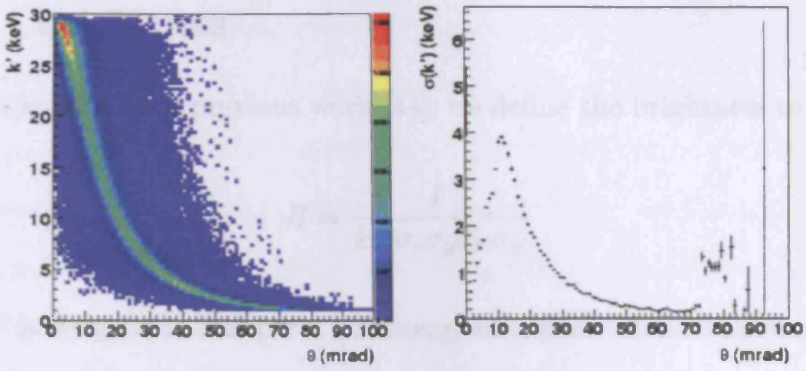

(a) Photon distribution in terms of energy and angle of scattering. cf Fig. 2.3.

(b) Photon rms energy spread as a function of angle of emission.

Figure 6.20: Scattered photon energies and rms energy spread. The value of each point in Figure (b) is the σ which results from fitting a Gaussian to each vertical bin in (a). The energy cut of $k' > 1$ keV causes the fit to fail above angles of around 80 mrad, so the energy spread in this region appears larger than the true value.

with a laser of wavelength 800 nm and the scattered photons are propagated 5 m to a detector plane, with a cut on the photon energy of 1 keV. The cross section for the interaction is normalised to 1 in BDSIM, so that each electron produces 1 photon. We generate 500000 events in order to produce a smooth distribution — as shown above, one bunch produces approximately $2.5 \cdot 10^7$ photons so these distributions represent 2 % of the scattering from one bunch crossing. The resulting photon distributions at a plane 5 m from the interaction point are displayed in Figs. 6.18, 6.19 and 6.20.

6.4.1 Brightness

For comparison with previous work [44], we define the brightness to be:

$$B = \frac{F}{4\pi^2 \sigma_x \sigma_y \sigma_{x'} \sigma_{y'}} \tag{6.7}$$

where F is the photon flux per 0.1 % energy bandpass. Table 6.10 summarises the photon yield and time-averaged brightness for several X-ray sources, while Tables 6.11 and 6.12 give the parameters for the modified ERLP and those of the Pleiades dedicated inverse Compton source for comparison. The values

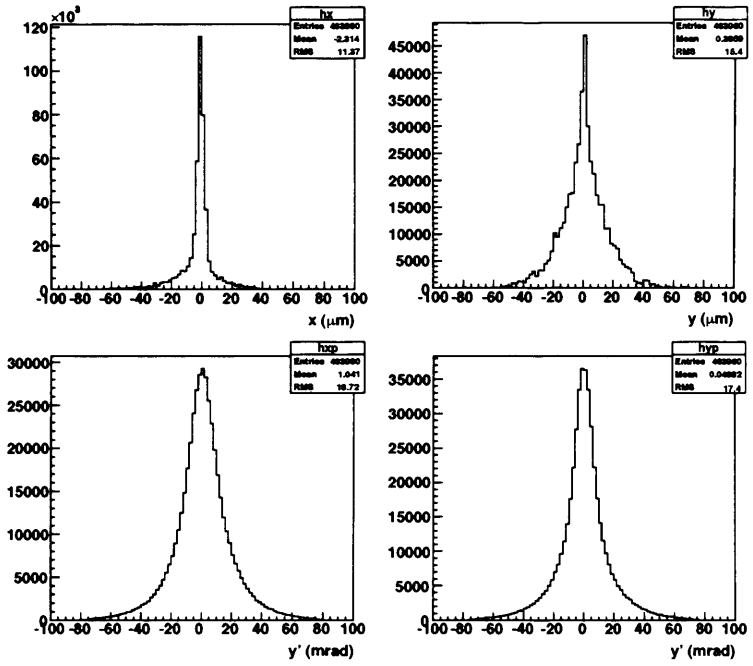

Figure 6.21: Scattered photon bunch distributions at the interaction point in (top left) x, (top right) y, (bottom left) x' and (bottom right) y'. We find rms values for these of 11.37 μm, 15.4 μm, 18.72 mrad and 17.4 mrad respectively.

of $\sigma_{x^{(\prime)},y^{(\prime)}}$ are taken from the scattered photon distribution at the interaction point, as modelled in BDSIM, (see Fig. 6.21). We see from Table 6.10 that the time-averaged brightness of the modified ERLP Compton source will be approximately three times greater than was initially achieved at Pleiades [50]. However, the planned Pleiades source upgrade is intended to reduce the electron beam spot size to 15 × 15 μm, and to increase the photon yield by a factor of 100. This should boost the time-averaged brightness by a factor of 200.

Source	Photons per bunch per (0.1 % b.p.)	Time-averaged brightness per (mm^2 mrad^2 s 0.1 % b.p.)
ERLP 300 × 300 μm	15	2.1
4GLS	$1.4 \cdot 10^3$	$3.5 \cdot 10^5$
Vanderbilt Uni	$1 \cdot 10^8$	$6.3 \cdot 10^5$
Pleiades (initial run)	$1.3 \cdot 10^3$	$5.8 \cdot 10^4$
Pleiades (upgrade)	$1 \cdot 10^5$	$2.5 \cdot 10^7$
JLab	0.017	$4.8 \cdot 10^3$
ERLP 14 × 20 μm	$4.14 \cdot 10^4$	$1.83 \cdot 10^5$

Table 6.10: Summary of the photon yield and time-averaged brightness for different inverse Compton scattering X-ray sources. These values have been collated from [44], and are presented here for ease of comparison.

6.5 Summary

Given the limitations in the specifications taken for the ERLP X-ray source, it is clear that the overall performance should be able to exceed that which has been achieved in the initial run of the Pleiades experiment. The overall limit on the brightness is set by the intrinsic spot size of the ERLP, which is limited by the design requirements for the energy recovery FEL mode.

	$1/2\gamma$ collection	Full collection
Maximum Photon Energy	29 keV	29 keV
Minimum pulse length (rms)	155 fs	155 fs
Time-averaged Flux (N_γ/s/0.1% b.p.)	$4.14 \cdot 10^5$	$1.25 \cdot 10^5$
Photons per bunch/0.1% b.p.	$4.14 \cdot 10^4$	$1.25 \cdot 10^4$
Repetition Frequency	10 Hz	10 Hz
Bandpass	15 %	200 %
Time-averaged/Peak Brightness (N_γ/mm^2/mrad^2/s/0.1% b.p.)	$1.83 \cdot 10^5/1.18 \cdot 10^{17}$	$5.54 \cdot 10^4/3.57 \cdot 10^{16}$
Divergence	18.7 × 17.4 mrad	18.7 × 17.4 mrad
Source Size	11.4 × 15.4 μm	11.4 × 15.4 μm
Laser, Time averaged power	8 W (0.8 J, 10 Hz)	8 W (0.8 J, 10 Hz)
Laser wavelength	800 nm	800 nm
Electron Energy	35 MeV	35 MeV
Electron Bunch Charge	80 pC	80 pC

Table 6.11: Parameter table for an ERLP inverse Compton source based on simulation in `elegant` and BDSIM, (see Fig. 6.21).

Maximum Photon Energy	70–78 keV
Minimum pulse length	2 ps (300 fs for reduced charge)
Time-averaged Flux (N_γ/s/0.1% b.p.)	$1.3 \cdot 10^4$
Photons per bunch/0.1% b.p.	$1.3 \cdot 10^3$
Repetition Frequency	10 Hz (assumed)
Bandpass	100 %
Time-averaged/Peak Brightness (N_γ/mm^2/mrad^2/s/0.1% b.p.)	$5.8 \cdot 10^4/2.9 \cdot 10^{15}$
Divergence	3 × 4.7 mrad
Source Size	20 × 20 μm (laser) 50 × 50 μm (electron)
Laser, Time averaged power	2 W (0.2 J, 10 Hz)
Laser wavelength	820 nm
Electron Energy	54–57 MeV
Electron Bunch Charge	270 pC

Table 6.12: Parameter table for the Pleiades inverse Compton source [50]. The Pleiades source collects a half-angle of $3/2\gamma$.

CHAPTER 7

Summary

Laserwire Studies

In the preceding chapters we have shown that the scattered radiation from laser-electron interactions can be used as a diagnostic tool in electron accelerators. The work with the PETRA Laserwire system has demonstrated the ability to measure beam sizes of order 100 μm (Fig. 4.23 and Fig. 4.28) using a laser beam focused to a spot size of 35 μm. Although the inclusion of a beampipe window has allowed a decrease in scanning time from 45 minutes down to 30 s, (Sec. 4.8.4) this is still insufficient for use in the ILC, where intra-train scanning will require scan times of order 100 μs for a single scan. Requiring multiple scans within a train will limit the available scanning time proportionally. To this end, further research is ongoing to generate a beam scanning system capable of operating at a rate of tens of kiloHertz [51]. Work is also in progress at the ATF facility in KEK to demonstrate the ability to focus a laser beam to micron spot sizes. In combination, the use of fast scanning and micron beam sizes could allow the use of a Laserwire system as an intra-train beam size monitor in the ILC at any location prior to the

Interaction Region.

ERLP Studies

Two particular features of inverse Compton scattering make this process an interesting source of radiation for user experiments: the tunability of the peak photon energy and the correlation between angular acceptance and bandwidth. In order to make this a viable source of radiation at the ERLP, it has been necessary to demonstrate that an inverse Compton source could be designed which would generate radiation with a high brightness. By optimally modifying the quadrupole strengths of the ERLP in the section between the bunch compressor and the selected interaction point, the electron bunch spot size can be reduced to 13.45×19.81 μm (Table 6.9). Calculations show that with a laser focused to an rms spot size of 20 μm, a photon flux of order 10^7 γ/BX can be achieved (Fig. 6.12). Based on these numbers, the calculated time-averaged brightness of the ERLP inverse Compton source has been shown to be comparable with that which can be achieved at other inverse Compton sources (Table 6.10). In addition, the ultra-short bunches (of order 100 fs) which can be generated lead to a peak brightness several orders of magnitude greater than can be achieved with standard wiggler synchrotrons (Fig. 5.1 and Table 6.11).

APPENDIX A

Derivation of Klein-Nishina Formula for Compton Scattering Cross Section

Compton scattering is the absorption and subsequent emission of a photon from an electron[1]. If the incident photon absorbed by the electron at one vertex can be represented by

$$A_\mu(x,k) = \frac{1}{\sqrt{2kV}}\epsilon_\mu(e^{-ik\cdot x} + e^{ik\cdot x}) \tag{A.1}$$

then the photon emitted at the second vertex is

$$A'_\mu(x',k') = \frac{1}{\sqrt{2k'V}}\epsilon'_\mu(e^{-ik'\cdot x'} + e^{ik'\cdot x'}) \tag{A.2}$$

This process conserves energy and momentum according to

$$k + p_i = k' + p_f \tag{A.3}$$

[1]This derivation is included for completeness, and is taken largely from [52].

where k and k' are the 4-momenta of the incident and emitted photons, and $p_{i,f}$ are those of the electron in its initial and final states.

By inserting (A.1) and (A.2) into the second order S-matrix and taking the Fourier transform into momentum space, we get

$$S_{fi} = \frac{e^2}{V^2}\sqrt{\frac{m^2}{E_f E_i}}\frac{1}{\sqrt{2k\cdot 2k'}(2\pi)^4\delta^4(p_f+k'-p_i-k)} \times\bar{u}(p_f,s_f)\left[(-i\not{\epsilon}')\frac{i}{\not{p}_i+\not{k}-m}(-i\not{\epsilon}) + (-i\not{\epsilon})\frac{i}{\not{p}_i-\not{k}'-m}(-i\not{\epsilon}')\right]u(p_i,s_i) \tag{A.4}$$

which describes the Feynman diagrams of Fig. A.1. Three terms with a δ^4-function requiring 4-momenta conditions which do not apply in this interaction[2] have been dropped.

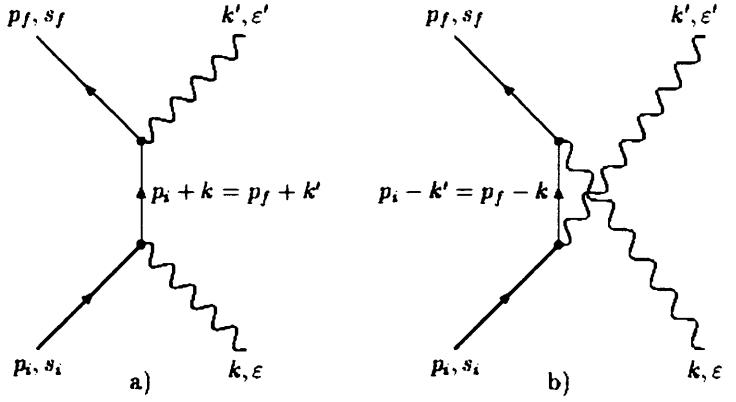

Figure A.1: The two first order diagrams for Compton scattering. These correspond to the terms in Eq. A.4, where the denominator equals a) $\not{p}_i + \not{k} - m$, and b) $\not{p}_i - \not{k}' - m$.

The cross section $d\sigma$ is then formed by taking the square of the amplitude of Eq. A.4, diving by $(2\pi)^4\delta^4(0)$ to form a rate, dividing by the incident flux

[2]These conditions are $p_i = p_f + k + k'$ and $p_f = p_i + k + k'$, which are impossible to satisfy, and $k' + p_i = k + p_f$ which cannot be simultaneously satisfied with our original condition in (A.3)

$|\boldsymbol{v}|/V$ and by the number of target particles per unit volume $1/V$. We then sum over the phase space $[V^2/(2\pi)^6 d^3p_f d^3k']$ to get

$$\begin{aligned} d\sigma = & \frac{e^4 m}{(2\pi)^2 2kE_i|v|} \\ & \times \int \left| \bar{u}(p_f, s_f) \left(\not{\epsilon}' \frac{1}{\not{p}_i + \not{k} - m} \not{\epsilon} + \not{\epsilon} \frac{i}{\not{p}_i - \not{k}' - m} \not{\epsilon}' \right) u(p_i, s_i) \right|^2 \\ & \times \delta^4(p_f + k' - p_i - k) \frac{m d^3 p_f}{E_f} \frac{d^3 k'}{2k'} \end{aligned} \tag{A.5}$$

In the laboratory frame where the electron is initially at rest, $m/kE_i|\boldsymbol{v}|$ is $1/k$, and the integral of all photons scattered into solid angle $d\Omega_{k'}$ about an angle θ gives

$$d\Omega_{k'} \int \frac{k'^2 dk'}{2k'} \int \frac{m\, d^3 p_f}{E_f} \delta^4(p_f + k' - p_i - k) \tag{A.6}$$

$$= m\, d\Omega_{k'} \int_0^\infty k' dk' \delta([k + p_i - k']^2 - m^2) \theta(k + m - k') \tag{A.7}$$

$$= m\, d\Omega_{k'} \int_0^{k+m} k' dk' \delta[2m(k - k') - 2kk'(1 - \cos\theta)] \tag{A.8}$$

$$= \frac{k'^2}{2k} d\Omega_{k'} \tag{A.9}$$

where we have used the identity

$$\frac{d^3 p}{2E} = \int_0^\infty dp_0 \delta(p_\mu p^\mu - m^2) d^3 p = \int_{-\infty}^\infty d^4 p \delta(p_\mu p^\mu - m^2) \theta(p_0)$$

$$\theta(p_0) = \begin{cases} 1 & \text{for } p_0 > 0 \\ 0 & \text{for } p_0 < 0 \end{cases}$$

We notice that the δ-function in Eq. A.9 requires that

$$k' = \frac{k}{1 + (k/m)(1 - \cos\theta)} \tag{A.10}$$

which is the same as the derived kinematic requirements from Eq. 2.5 when the electron is at rest: that is, $\beta = 0$ and $\alpha = \pi$. From this, Eq. A.5 reduces to

$$\frac{d\sigma}{d\Omega} = \alpha^2 \left(\frac{k'}{k}\right)^2 \left| \bar{u}(p_f, s_f) \left(\not{\epsilon} \frac{1}{\not{p}_i + \not{k} - m} \not{\epsilon} + \not{\epsilon} \frac{i}{\not{p}_i - \not{k}' - m} \not{\epsilon}' \right) u(p_i, s_i) \right|^2 \tag{A.11}$$

which describes the cross section when both electron and photon are polarised in the initial and final states. By choosing a gauge in which the initial and final photons are transversely polarised in the laboratory frame so that

$$\epsilon^\mu = (0, \boldsymbol{\varepsilon}) \quad \text{with } \boldsymbol{\varepsilon} \cdot \boldsymbol{k} = 0$$
$$\epsilon^{\mu\prime} = (0, \boldsymbol{\varepsilon}') \quad \text{with } \boldsymbol{\varepsilon}' \cdot \boldsymbol{k}' = 0$$

We find that $\epsilon \cdot p_i = \epsilon' \cdot p_i = 0$ and the spinor factors become

$$\bar{u}(p_f, s_f) (\cdots) u(p_i, s_i) = -\bar{u}(p_f, s_f) \left(\frac{\not{\epsilon}' \not{\epsilon} \not{k}}{2k \cdot p_i} + \frac{\not{\epsilon} \not{\epsilon}' \not{k}'}{2k' \cdot p_i} \right) u(p_i, s_i) \tag{A.12}$$

where we have used the properties of Dirac spinors such that:

$$(\not{p}_i + m)\ \not{\epsilon} u(p_i, s_i) = \not{\epsilon}(-\not{p}_i + m) u(p_i, s_i) = 0 \tag{A.13}$$

Combining this with Eq. A.11, we then take the sum over final spins s_f and average over the initial spins s_i to obtain the cross section for an unpolarised

electron.

$$\frac{d\bar{\sigma}}{d\Omega} = \frac{1}{2}\sum_{\pm s_i, s_f} \frac{d\sigma}{d\Omega} \tag{A.14}$$

$$= \frac{\alpha^2}{2}\left(\frac{k'}{k}\right)^2 \mathrm{Tr}\,\frac{\not{p}_f + m}{2m}\left(\frac{\not{\epsilon}\not{\epsilon}'\not{k}}{2k\cdot p_i} + \frac{\not{\epsilon}'\not{k}'}{2k'\cdot p_i}\right)\frac{\not{p}_i + m}{2m} \tag{A.15}$$
$$\times\left(\frac{\not{k}\not{\epsilon}\not{\epsilon}'}{2k\cdot p_i} + \frac{\not{k}'\not{\epsilon}'\not{\epsilon}}{2k'\cdot p_i}\right)$$

This leaves three distinct traces to be evaluated, as the cross terms with denominator $(k\cdot p_i)(k'\cdot p_i)$ are identical by Trace theorem 6 [3].

$$T_1 = \mathrm{Tr}\,(\not{p}_f + m)\ \not{\epsilon}\ \not{\epsilon}\ \not{k}(\not{p}_i + m)\ \not{k}\ \not{\epsilon}'\ \not{\epsilon}' \tag{A.16}$$

$$= \mathrm{Tr}\ \not{p}_f\ \not{\epsilon}\ \not{\epsilon}\ \not{k}\ \not{p}_i\ \not{k}\ \not{\epsilon}'\ \not{\epsilon}' \tag{A.17}$$

$$= \mathrm{Tr}\, 2k\cdot p_i\ \not{p}_f\ \not{\epsilon}\ \not{\epsilon}\ \not{k}\ \not{\epsilon}'\ \not{\epsilon}' \tag{A.18}$$

$$= 8k\cdot p_i(k\cdot p_f + 2k\cdot\epsilon' p_f\cdot\epsilon') \tag{A.19}$$

$$= 8k\cdot p_i\left[k'\cdot p_i + 2(k\cdot\epsilon')^2\right] \tag{A.20}$$

where terms proportional to m^2 vanish because $k^2 = 0$ and we have used Trace theorems 1[4] and 3[5]. We can then evaluate:

$$T_2 = \mathrm{Tr}\,(\not{p}_f + m)\ \not{\epsilon}\ \not{\epsilon}'\ \not{k}'(\not{p}_i + m)\ \not{k}'\ \not{\epsilon}'\ \not{\epsilon} \tag{A.21}$$

in a similar way, noticing that this differs from T_1 only by the substitution

[3] $\mathrm{Tr}[\not{a}_1\ \not{a}_2\cdots\not{a}_{2n}] = \mathrm{Tr}[\not{a}_{2n}\cdots\not{a}_2\ \not{a}_1]$
[4] $\mathrm{Tr}[\not{a}_1\cdots\not{a}_n] = a_1\cdot a_2\mathrm{Tr}[\not{a}_3\cdots\not{a}_n] - a_1\cdot a_3\mathrm{Tr}[\not{a}_2\ \not{a}_4\cdots\not{a}_n] + \cdots + a_1\cdot a_n\mathrm{Tr}[\not{a}_2\cdots\not{a}_{n-1}]$
[5] $\mathrm{Tr}[\not{a}_1\cdots\not{a}_n] = a_1\cdot a_n\mathrm{Tr}[\not{a}_2\cdots\not{a}_{n-1}]$

$\epsilon, k \leftrightarrow \epsilon', -k'$ and so:

$$T_2 = 8k' \cdot p_i \left[k \cdot p_i + 2(k' \cdot \epsilon)^2\right] \tag{A.22}$$

For the last trace, we find:

$$T_3 = \mathrm{Tr}\,(\not{p}_f + m)\ \not{\epsilon}\ \not{\epsilon}\ \not{k}(\not{p}_i + m)\ \not{k}'\ \not{\epsilon}\ \not{\epsilon} \tag{A.23}$$

$$= \mathrm{Tr}\,(\not{p}_i + m)\ \not{\epsilon}\ \not{\epsilon}\ \not{k}(\not{p}_i + m)\ \not{k}'\ \not{\epsilon}\ \not{\epsilon} + \mathrm{Tr}\,(\not{k} - \not{k}')\ \not{\epsilon}\ \not{\epsilon}\ \not{k}\ \not{p}_i\ \not{k}'\ \not{\epsilon}\ \not{\epsilon} \tag{A.24}$$

$$= \mathrm{Tr}\,(\not{p}_i + m)\ \not{k}(\not{p}_i + m)\ \not{k}'\ \not{\epsilon}\ \not{\epsilon}\ \not{\epsilon}\ \not{\epsilon} + 2k \cdot \epsilon'\,\mathrm{Tr}\,(-1)\ \not{k}\ \not{p}_i\ \not{k}'\ \not{\epsilon} \tag{A.25}$$
$$-2k' \cdot \epsilon\,\mathrm{Tr}\,(-1)\ \not{\epsilon}\ \not{k}\ \not{p}_i\ \not{k}'$$

$$= 2k \cdot p_i\,\mathrm{Tr}\ \not{p}_i\ \not{k}'\ \not{\epsilon}\ \not{\epsilon}\ \not{\epsilon}\ \not{\epsilon} - 8(k \cdot \epsilon')^2 k' \cdot p_i + 8(k' \cdot \epsilon)^2 k \cdot p_i \tag{A.26}$$

$$= 8(k \cdot p_i)(k' \cdot p_i)\left[2(\epsilon' \cdot \epsilon)^2 - 1\right] - 8(k \cdot \epsilon')^2 k' \cdot p_i + 8(k' \cdot \epsilon)^2 k \cdot p_i \tag{A.27}$$

Putting these traces into Eq. A.15, we have the Klein-Nishina [1] formula for Compton scattering:

$$\frac{d\bar{\sigma}}{d\Omega} = \frac{\alpha^2}{4m^2}\left(\frac{k'}{k}\right)\left[\frac{k'}{k} + \frac{k}{k'} + 4(\epsilon' \cdot \epsilon)^2 - 2\right] \tag{A.28}$$

with k and k' related by the scattering angle according to Eq. A.10. Finally, we sum over the final photon polarisations ϵ', average over the initial photon polarisations ϵ, and integrate about the azimuthal angle for the unpolarised cross section:

$$\frac{d\bar{\sigma}}{d\cos\theta} = \pi r_e^2\left(\frac{k'}{k}\right)\left[\frac{k'}{k} + \frac{k}{k'} - 1 + \cos^2\theta\right] \tag{A.29}$$

References

[1] O. Klein and Y. Nishina, *Z. Physik,* **52** , 853 (1929)

[2] K. Chouffani *et al, "Determination of electron beam parameters by means of laser-Compton scattering"*, Physical Review Special Topics - Accelerators and Beams, **9**, 050701 (2006)

[3] L. D. Landau and E. M. Lifshitz, *"Classical Theory of Fields"*(Butterworth-Heinemann, Oxford, U. K. 1975) 4th Ed.

[4] F. V. Hartemann *et al, "High-energy scaling of Compton scattering light sources"*, Physical Review Special Topics - Accelerators and Beams, **8**, 100702 (2005)

[5] "ILC Wiki, Reference Design Report "
http://www.linearcollider.org/wiki/doku.php?id=rdr:rdr_home

[6] "The International Linear Collider Global Design Effort Baseline Configutation Document"
http://www.linearcollider.org/wiki/doku.php?id=bcd:bcd_home

[7] G. Guignard and R. W. Assmann., *"A 3 TeV e^+e^- Linear Collider based on CLIC Technology"*, Geneva: CERN, 2000.

[8] H. Braun *et al, "Status of CLIC High-Gradient"*, Proceedings of the Particle Accelerator Conference, 2001, Chicago, Illinois

[9] A. Brachmann *et al, "The Polarized Electron Source for the International Collider (ILC) Project"* , SLAC-PUB-1238, Proceedings of the 17th International Spin Physics Symposium, 2006, Kyoto, Japan

[10] Y. Ivanyushenov *et al, "Development of a Superconducting Helical Undulator for the ILC Positron Source"*, Cockcroft-06-35, Proceedings of the European Particle Accelerator Conference 2006, Edinburgh, UK

[11] A. Wolski *et al, "Choosing a Baseline Configuration for the ILC Damping Rings"*, Proceedings of the European Particle Accelerator Conference 2006, Edinburgh, UK

[12] H. Hayano, *"Progress and Plans for R&D and the Conceptual Design of the ILC Main Linacs"*, Proceedings of Particle Accelerator Conference 2005, Knoxville, Tennessee

[13] A. Seryi, *"The ILC Beam Delivery System — Conceptual Design and R&D Plans"*, Proceedings of Particle Accelerator Conference 2005, Knoxville, Tennessee

[14] Y. Nosochkov *et al , "Design of Extraction Line Optics for the ILC Interaction Regions with 20 mrad and 2 mrad Crossing Angles"*, Proceedings of International Linear Collider Workshop 2005, Stanford, California

[15] H. Wiedemann, *"Particle Accelerator Physics: Basic Principles and Linear Beam Dynamics"* (Springer-Verlag, Berlin Heidelberg, 1993)

[16] M. Ross *et al*, *"Wire Scanners for Beam Size and Emittance Measurements at the SLC"*, SLAC-PUB 5556, May 1991

[17] Physics and Detector for LC in Zeuthen, http://www-zeuthen.desy.de/ILC/beam/wirescanner.html

[18] DESY TTF Home Page, http://tesla.desy.de/TTF_intro.html

[19] R. Assman *et al*, *"Design Status of the CLIC 3-TeV Beam Delivery System and Damping Rings"*, CERN-SL-2000-058-AP

[20] P. Tenembaum *et al*, *"New Delevopments to the Next Linear Collider Beam Delivery System Design"* , SLAC-PUB-8135, Proceedings of Particle Accelerator Conference 1999, New York, NY

[21] R. Brinkmann *et al*, *"A New Beam Delivery System for the TESLA Linear Collider"*, DAPNIA-SEA-00-04

[22] M. Placedi *et al*, *"Design and First Performance of the LEP Polarimeter"*, Proceedings of the European Particle Accelerator Conference 1990, Nice, France

[23] National Instruments, LabView website, http://www.ni.com/labview/

[24] The ROOT Collaboration, *"ROOT: An Object-oriented Data Analysis Framework"* http://root.cern.ch

[25] J. Keil, HERA Beam Dynamics Seminar, July 2003

[26] J. C. Carter, *"Beam Position Readout System for the LBBD Project"*, MSc thesis, Royal Holloway University of London, September 2003

[27] K. Balewski *et al*, *"Simulation and Background Measurements for a Laser Based Beam Size Monitor for the Future Linear Collider"*, Proceedings of Particle Accelerator Conference 2001, Chicago, Illinois

[28] F. Poirier, *"Beam Diagnostic Laser-wire and Fast Luminosity Spectrum Measurement at the International Linear Collider"*, PhD thesis, Royal Holloway University of London, July 2005

[29] G. Blair *et al*, *"R&D Towards a Laser Based Beam Size Monitor for the Future Linear Collider"* , Proceedings of the European Particle Accelerator Conference 2002, Paris, France

[30] S. Boogert , *"CCD Diagnostics and 04/12/2003 Data"*, Presentation to Laserwire collaboration meeting, Oxford, 24/01/2004

[31] K. Balewski *et al*, *"Beam Profile Measurements at PETRA with the Laserwire Compton Scattering Monitor"*, Proceedings of the European Particle Accelerator Conference 2004, Lucerne, Switzerland

[32] BDSIM Web Page. http://flc.pp.rhul.ac.uk/bdsim.html

[33] j. C. Carter, *"Laserwire Simulation Update"* , Presentation to Laserwire Collaboration meeting, 18th November 2004

[34] J. C. Carter, *"Particle Physics and Beam-line Studies for the Electron-Positron International Linear Collider"*, PhD thesis, Royal Holloway University of London, October 2006

[35] J. Carter *et al*, *"Beam Profile Measurements and Simulations of the PETRA Laser-Wire"*, Proceedings of Particle Accelerator Conference 2005, Knoxville, Tennessee

[36] S. Boogert, *"Extraction Line Laserwire Summary"*, Presentation to the 3rd TB & SGCs Joint Meeting, 20th December 2006

[37] M. Price *et al*, *"Beam Profile Measurements with the 2-D Laserwire"*, Proceedings of the European Particle Accelerator Conference 2006, Edinburgh, UK

[38] P. Tenenbaum & T. Shintake, *"Measurement of Small Electron-Beam Spots"* , Annu. Rev. Nucl. Part. Sci. 1999. 49:125-62

[39] T. Shintake *et al*, *"Experiments of Nanometer Spot Size Monitor at FFTB Using Laser Interferometry"*, SLAC-PUB-1238, Proceedings of the Particle Accelerator Conference, 1995, Dallas, Texas

[40] D. Moncton, *"High-Brilliance Compact X-ray Sources: Micron Source Size and Pico-Second Pulses"*, Seminar presentation, UCL, Nov 2005

[41] Bending magnet energy spectrum calculator, Centre for X-Ray Optics, Lawrence Berkley Laboratory.
http://www-cxro.lbl.gov/optical_constants/bend2.html

[42] V. Ayvazyan *et al, "First operation of a free-electron laser generating GW power radiation at 32 nm wavelength"*, Eur. Phys. J. D **37**, 297-303 (2006), DOI: 10.1140/epjd/e2005-00308-1

[43] 4GLS Conceptual Design Report, http://www.4gls.ac.uk

[44] M. MacDonald, *"Report into the production of X-rays from the ERL Prototype through Thompson Scattering (Compton Back-scattering)"*, 4GLS note, dev-xray-thom-rpt-001, 30th June 2005

[45] H. Owen and B. Munatori, *"Compton Backscattering in ERLP"*, 4GLS note, erlp-desn-rpt-0036, 17th March 2005

[46] The MAD8 homepage, http://mad.home.cern.ch/mad/mad8web/mad8.html

[47] H. Owen, *"ERLP Magnets and Diagnostics Specification"*, 4GLS note, erlp-desn-rpt-0016, 9th December 2003

[48] M. Borland, *"elegant: A Flexible SDDS-Compliant Code for Accelerator Simulation"*, Advanced Photon Source LS-287, September 2000

[49] H. Owen, Daresbury Laboratories. Private communication

[50] D. Gibson *et al, "PLEIADES: A picosecond Compton scattering X-ray source for advanced backlighting and time-resolved material studies"*, Phys. Plasmas **11(5)**, pp2857–284, 2004

[51] A. Bosco,*et al, "Proposal for a Fast Scanning System based on ElectroOptics for use at the ILC Laser-Wire"*,Proceedings of the European Particle Accelerator Conference 2006, Edinburgh, UK

[52] J. D. Bjorken and S. D. Drell, *"Relativistic Quantum Mechanics"*, (McGraw-Hill Book Company, 1964)